MODELING THE EFFECTS OF CONVECTIVE DOWNDRAFTS ON THE GLOBAL CIRCULATION OF THE ATMOSPHERE

by Ching-Hsuan Chen

David A. Randall, Principal Investigator

Colorado State University

DEPARTMENT OF ATMOSPHERIC SCIENCE

PAPER NO. 591

MODELING THE EFFECTS OF CONVECTIVE DOWNDRAFTS ON THE GLOBAL CIRCULATION OF THE ATMOSPHERE

by

Ching-Hsuan Chen

Research supported by the
National Science Foundation
under grant numbers ATM-9121629 and ATM-9214981
and by the
U.S. Department of Energy
under grant number DE-FG03-94ER91629

Department of Atmospheric Science
Colorado State University
Fort Collins, CO

November 1995

Atmospheric Science Paper No. 591

Abstract

We have adopted Johnson's approach to construct an updraft-downdraft ensemble model as an extension of the prognostic Arakawa-Schubert cumulus parameterization. The downdraft parameterization is used to determine the effects of downdrafts on temperature, moisture, and momentum. It has been tested in extended simulations with the Colorado State University General Circulation Model. Comparisons between simulations with the updraft-only parameterization and with the updraft-downdraft parameterization reveal several improvements. These include: (1) a more realistic global precipitation pattern and cloud distribution; (2) a cooler and more humid tropical troposphere; and (3) a relatively well-defined easterly jet in the upper troposphere of the Indian summer monsoon region. Downdrafts tend to moisten and cool the lower cloud layer, thus enhancing the convective instability of the cumulus environment and generating more lower-tropospheric clouds. They also dry the boundary layer, by injecting dry air. In strongly convective regions, convective downdrafts increase the surface sensible and latent heat fluxes.

1. Introduction

Cumulus clouds, whether precipitating or nonprecipitating, usually have their roots in the planetary boundary layer (PBL), and so their properties strongly depend on the characteristics of the boundary-layer air. The clouds feed back to modify both the boundary layer and the cloud layer through transports, precipitation, and modulation of the shortwave and longwave radiative fields. In order to understand the interactions between cumulus clouds and the PBL, studies of the transformation of the boundary layer by deep convective activity have received considerable attention in the past two decades.

Convective updrafts lead to condensation and production of precipitation. Convective downdrafts induced by the precipitation loading and evaporation of precipitation falling outside the cloudy updraft were recognized during the Thunderstorm Project (Byers and Braham, 1949). Subsequent observational investigations provided measurements of in-cloud downdraft properties and of outflow thermodynamics. Zipser (1969), Echternacht and Garstang (1976), Betts (1976) and others emphasized that the downdrafts replace warm, moist subcloud layer air by cool dry air. Betts (1976), Miller and Betts (1977), and Betts and Silva Dias (1979) carried out some pioneering research aimed at understanding the dynamics and thermodynamics of downdrafts. Recently, indirect observations (multiple Doppler radar, surface mesonet, radiosonde and photography) data (Fankhauser et al. 1982; Wade and Foote, 1982; Fujita and Wakimoto, 1981; Klemp et al., 1981;Ogura and Liou, 1980) and conceptual modeling (Foote and Frank, 1983; Knupp and Cotton, 1982 a; Heymsfield, 1981) studies have further documented convective storm properties. However, the mechanisms which govern downdraft structure and dynamics remain rather unknown.

Many observational studies have shown that convective-scale downdrafts are important for tropical cloud clusters (Zipser, 1977; Houze, 1977; Houze and Betts, 1981) and long-lived squall systems in a sheared environment (Newton, 1966; Ludlam, 1963; Takeda, 1971), in several respects. Downdrafts produce strong vertical transports of static energy, mass and momentum within and near precipitating convective clouds, particularly at low levels. Such transports can significantly modify the mean state of the PBL and, indirectly, the surface fluxes. In addition, downdraft transports of mass and momentum can produce low- level gust fronts which influence the propagation of individual convective clouds and the development of new clouds. Molinari and Corsetti (1985) have shown that downdrafts sharply increase the grid-scale static stability by injecting cold dry air into the boundary layer. The near-surface cooling by downdrafts has also been confirmed by observations. For example, GATE observations reveal downdraft-driven cooling of about 2 K (Barnes and Garstang, 1982). In the TOGA COARE (Tropical Ocean Global Atmosphere Coupled Ocean-Atmosphere Response Experiment) region, cumulus convection has been found to reduce the near-surface air temperature by about 4 to 6 K (Young et al., 1992). These studies suggest that a convective downdraft parameterization is necessary for large-scale models. They also indicate that cumulus and PBL parameterizations must be coupled, if the interaction between cumulus convection and the PBL is to be realistically simulated.

This paper reports the development of a combined updraft-downdraft cumulus ensemble model within the framework of the prognostic Arakawa-Schubert cumulus parameterization (Randall and Pan 1993) used in the Colorado State University (CSU) general circulation model (GCM). In the following section, we summarize the effects of convective downdrafts on the cloud-layer environment, boundary layer, and surface fluxes. Section 3 reviews the convective-downdraft parameterizations so far proposed, and their applications in GCMs. Section 4 describes the design of our numerical experiments. The effects of the convective downdrafts on the global circulation of the atmosphere are analyzed in Section 5. Section 6 summarizes our results and suggests future directions.

2. The effects of downdrafts

2.1 *Cloud layer*

The effects of mesoscale updrafts and downdrafts on the large-scale energy budget have been studied by several authors. Houze (1982) and Johnson and Young (1983) calculated the energy budget of a large-scale area containing an idealized cloud cluster. They found that strong heating due to condensation in the mesoscale updraft occurs above 5 km, while cooling associated with melting and evaporation in the mesoscale downdraft occurs in the lower layer. Cheng (1989), used a diagnostic cumulus ensemble model to examine the effects of convective scale downdrafts on the large-scale energy and moisture budgets of tropical convective systems. He found that downdrafts tend to cool and moisten the environment and that the contributions of downdrafts to the apparent non-radiative energy source Q_1-Q_R and the apparent moisture sink Q_2 (Yanai et al. 1973) are comparable, in the lower atmosphere, to the contributions of updrafts. He found that the cooling and moistening due to the downdrafts are strongest near cloud base. Wu (1992) applied Cheng's model to the PRE-STORM data set, to examine the effects of convective-scale downdrafts on the large-scale energy and moisture budgets of midlatitude convective systems. He also found that convective-scale downdrafts tend to cool and moisten the lower troposphere. Near the cloud base, the cooling and moistening due to downdrafts was about half as strong as the heating and drying due to the updrafts.

Diagnostic studies by Johnson (1976) and Nitta (1977) showed that the inclusion of downdrafts substantially reduces the diagnosed mass flux of shallow clouds and the net cumulus mass flux near the cloud base. The opposite conclusion was reached by Cheng and Arakawa (1990), in a prognostic study.

2.2 *Subcloud layer*

Gray (1973), Yanai et al. (1973), Ogura and Cho (1973), Cho and Ogura (1974) and Nitta (1975) have estimated the contributions of the vertical transports associated with tropical cumulus clouds to the large-scale budgets of energy and moisture. They found that the total mass entering cumulus clouds through cloud base in weak tropical disturbances is one order of magnitude larger than the mass entering the subcloud layer through large-scale horizontal convergence. This excess mass is compensated for by the downward motions associated with cumulus clouds. The significance of this strong local circulation for the energy and moisture budgets of the subcloud layer is that a large amount of energy and moisture in the subcloud layer is lost into clouds updrafts. In the presence of convective downdrafts, the sinking air can penetrate directly into the subcloud layer, thus diluting the subcloud layer with potentially cool and dry air from aloft.

Zipser (1969) presented evidence that air from the tropical mid-troposphere descends to near the Earth's surface in mesoscale disturbances.

Since convective updrafts usually originate in the PBL, the interactions between cumulus convection and the PBL have the potential to influence not only the mean state and turbulent fluxes of the PBL, but also the evolution of convective activity itself. Many studies of both the tropics and mid-latitudes indicate that cumulus convection strongly modifies the thermodynamic properties of the PBL, which, in turn, play an important role in determining the buoyant energy available for cumulus convection.

As the cold downdraft air reaches the surface and spreads out, it enhances the activity of turbulent plumes rising from the relatively warm surface (Houze, 1977; Zipser, 1977; Gaynor and Mandics, 1978; Gaynor and Ropelewski, 1979). Thus, cumulus convection with both updrafts and downdrafts is more efficient in transporting the moist static energy upward in the troposphere than that with updrafts alone (Krueger, 1988, Cheng,1989).

Observational studies show that the mechanisms by which convection modifies the PBL include evaporation of precipitation falling through the PBL, as well as injection of downdraft outflows. Evaporation within the PBL of precipitation associated with downdrafts is discussed by Betts and Silva Dias (1979), Betts (1976, 1982), and Leary (1979). The effects of downdraft outflows in the PBL have been studied extensively for the tropics (Betts, 1976; Emmitt, 1978; Gaynor and Mandics, 1978; Gaynor and Ropelewski, 1979; Brummer, 1978; Johnson, 1981; Barnes and Garstang, 1982; and Sud, 1993) and for mid-latitudes (Charba, 1974; Goff, 1976;

Betts, 1984). These studies show that downdrafts often reach very close to the surface and effectively replace the mixed layer air. This leads to a modified PBL (sometimes called a "wake") with properties significantly different from those of the pre-convective PBL. The generation of such wakes leads to a surprisingly long-lasting significant large-scale, low-level stabilization. The observations suggest a simple two-layer structure in which the subcloud layer (in front of the mesoscale system) rises in updrafts and is replaced by air from the layer immediately above, which descends with the evaporation of precipitation in moist downdrafts (Betts, 1976). The study of Gaynor and Ropelewski (1979) indicates that mean wake duration during GATE was nearly 3 h, with some lasting over 16 h. Wakes were found to occupy an average of 30% of the GATE boundary layer. The process by which turbulent fluxes in the PBL to restore the wake region to pre-outflow conditions (often called "recovery" in the literature) has been modeled by Fitzjarrald and Garstang (1981) and Nicholls and Johnson (1984), who showed that over the tropical oceans wake recovery is dominated by buoyant turbulence and can be modeled successfully using a simple zero-order jump model. The outflow and recovery process thus acts to favor convective systems which propagate away the outflow region into the undisturbed PBL.

David (1992) investigated the impact of convective outflows on the air-sea interface, using measurements from the field phase of TOGA COARE. He showed a case with an outflow 3-5 K cooler than its environment, and a gust front of 8-10 m s^{-1}. These results and the discussion of Bradley et al. (1991) suggest that this type of system may be relatively common over the western Pacific warm pool, in association with modest convective events. In contrast, the climatological study by Barnes and Garstang (1982) showed that pools of air 2-3 K cooler than their environment were commonly observed over the GATE study area in the tropical Atlantic, but that significantly stronger events, such as the type observed in TOGA COARE, were relatively rare in GATE. A more detailed climatology of surface outflows is clearly needed.

2.3 Surface fluxes

Compared to the amount of effort dedicated to the study of downdraft effects on the mean state, relatively little attention has been directed to the effects of downdrafts on the surface fluxes. Variations in convectively induced cloud cover and precipitation were the main phenomena responsible for day-to day variations in the surface energy budget. In a modeling study, Sud (1993) showed that including the effects of downdrafts in a cumulus parameterization substantially enhances the surface fluxes. Young and Ledvina (1992) used observations from the tropical Western Pacific to show that convective downdrafts concurrent with precipitation events acted to cool the atmospheric boundary layer and thus to enhance the surface sensible and latent heat fluxes. There is a need for many more observational and modeling studies of the effects of convective downdrafts on the turbulent fluxes in the PBL; the TOGA COARE data set should be well suited to this purpose.

3. Downdraft parameterizations for GCMs

Three approaches have been developed to parameterize the effects of convective downdrafts in large-scale numerical models such as GCMs: (1) use of a simple cloud model (Johnson, 1976; Cheng,1989; Emanuel, 1991; Sud and Walker, 1993); (2) bulk methods (Tiedtke, 1989); and (3) relaxation methods (Betts and Miller, 1993).

An issue in the application of the "cloud model" approach is that it is not clear how detailed the cloud model must be in order to obtain realistic results; in particular it is presently uncertain whether the single components of the cloud spectrum must be described, or bulk representation is sufficient. Some evidence that a bulk model may be adequate for tropical convection has been provided by Yanai et al. (1976) who show that a bulk model and a spectral model give nearly identical results for the cloud mass flux, but little is known about cloud populations in other synoptic situations, such as mid-level convection in middle latitudes.

Johnson (1976) assumed that each type of updraft has an associated downdraft, which can be modeled as an inverted plume. In order to include downdraft plumes in his model, Johnson introduced two free parameters: the height of the top of the plume and the mass flux there. The results of his study indicated that cumulus downdrafts contribute significantly to the total convective mass transport in the lower troposphere. He showed that including cumulus downdrafts and the associated rainfall evaporation leads to the diagnosis of less shallow cumulus activity in highly convective situations. His results also show that downdraft water vapor transport is important for the water vapor balance of the subcloud layer.

Drawbacks of Johnson's approach include the lack of explicit descriptions of the properties of different downdrafts, and the use of free parameters that can significantly influence the results.

Cheng (1989 a, b) developed a much more comprehensive diagnostic cumulus ensemble model to determine the properties of downdrafts. He considered that the convective-scale downdrafts are initiated and maintained by the loading and evaporative cooling effects of rainwater which is generated in tilted updrafts. A unique feature of Cheng's parameterization is its ability to diagnose the tilting angle of updrafts from the observed thermodynamic fields. Cheng and Arakawa (1990) incorporated a downdraft parameterization into the Arakawa-Schubert cumulus parameterization. Their simulation experiments with the UCLA GCM show that the downdraft parameterization leads to several improvements of the results, including: 1) a more realistic global precipitation pattern; 2) a cooler and wetter tropical troposphere; and 3) a well-defined eastward-propagating low-frequency wave number 1 oscillation in the 200 mb zonal wind over the equator.

Emanuel (1991) formulated a representation of convective fluxes based on an idealized model of subcloud-scale updrafts and downdrafts. The downdraft mass fluxes in Emanuel's parameterization also follow from the updrafts, as Johnson (1976) does. However, the downdraft mass fluxes in Emanuel's parameterization are not only functions of the updraft mass fluxes, but also depend on the environmental moisture and temperature soundings. Emanuel also parameterized the unsaturated downdrafts.

Sud and Walker (1993) designed a rain evaporation and downdraft parameterization to complement the cumulus parameterization of the Goddard Laboratory for Atmospheres General Circulation Model (GLA GCM). They calculated downdraft mass fluxes emanating from different levels of the atmosphere by using an explicitly prescribed fraction of rain evaporation within the downdraft. A comparison of GLA GCM simulations of the annual cycle with and without downdrafts reveals that downdrafts make the sensible flux over the tropical oceans much more realistic (4-8 W m^{-2} larger) and reduce the excessive rainfall over the warm pool region of the tropical western Pacific. This finding is consistent with that of Cheng and Arakawa (1990).

Tiedtke (1989) employed a bulk model which is applied separately to various types of convection (cumulus updrafts, cumulus downdrafts, penetrative convection, shallow convection, and midlevel convection). Global integrations were performed with the model used for operational forecasts at ECMWF, and compared with results from en earlier version of the ECMWF model which uses a Kuo parameterization and represents shallow convection by vertical diffusion. Tiedtke's results indicate that the new parameterization provides more heating in the tropics and that the ascending branches of the Hadley cell over the West Pacific and Indian oceans are stronger and extend to higher levers than in the earlier version of the model.

Instead of using a cloud model, Betts and Miller (1993) relaxed simultaneously the temperature and moisture structures toward empirically prescribed reference structures, without considering the detailed process within the clouds. Their parameterization uses a specified relaxation time. The relaxation effectively determines both the vertically integrated heating and moistening, but the predictability of the temperature and water vapor profiles is limited by the use of empirically imposed profiles. Two distinct reference thermodynamic structures are used for shallow and deep convection. A separate reference profile was used to simulate downdraft effects and a separate adjustment time was used to simulate the modification of the boundary layer by downdrafts.

4. A simple convective downdraft parameterization

The Arakawa-Schubert cumulus parameterization is used in the CSU GCM (Arakawa and Schubert, 1974), with a prognostic closure as discussed by Randall and Pan (1993). In its original form, the parameterization does not include the effects of convective downdrafts. We have modified the cumulus parameterization to include them. The updraft-only version of this model is identical to the one dimensional cumulus ensemble model introduced by Randall and Pan (1993).

Convective-scale precipitation-driven downdrafts are parameterized following the method proposed by Johnson (1976).

The AS theory describes how the internal sounding of an individual cumulus cloud is controlled by the large-scale environment in which it grows. Multiple cloud types are permitted, and all clouds of a particular type are assumed to be identical. The convective updrafts are assumed to entrain environmental air between the PBL top and cloud top. Each subensemble is distinguished from the rest by its fractional entrainment rate λ which is assumed to be independent of height. The convective fluxes of sensible heat and moisture can be expressed in term of the convective mass flux and the differences between the in-cloud and environmental soundings. In the description of feedback, the large-scale tendencies due to a particular subensemble turn out to be proportional to the cumulus mass flux at cloud base for that subensemble. The distribution of the cloud-base mass flux over the various sub-ensembles is called the mass flux distribution function and is denoted by $M_B(\lambda)$. Randall and Pan (1993) proposed a prognostic closure to determine $M_B(\lambda)$.

Our downdraft parameterization follows the work of Johnson (1976), who assumed that each updraft has an accompanying downdraft, and that both have the same fractional mass entrainment rate. Johnson also assumed that the downdrafts originate at a level above cloud base and below cloud top, given by a certain specified fraction β of the pressure-depth of the corresponding updrafts. Johnson also employed an assumed relation between the downdraft-origination-level mass flux $M_0(\lambda)$ and the updraft-cloud-base mass flux $M_B(\lambda)$, $\frac{M_0(\lambda)}{M_B(\lambda)} = -\varepsilon(\lambda)$. We follow Johnson (1976) by choosing $\beta = 0.75$ and $\varepsilon(\lambda) = 0.2$. Results of a sensitivity study are described later in this paper.

We have extended Johnson's parameterization to include vertical momentum transport by the downdrafts; this parallels the vertical momentum transport by updrafts that has always been part of our model. To formulate the momentum transport by the downdrafts, we simply assume that momentum is conserved inside the downdrafts, so that the momentum in the downdrafts varies with height only as a result of entrainment.

The details of the downdraft parameterization are described in Appendix A.

5. Experiments with the CSU GCM

The core of the CSU GCM is based on a version of the UCLA GCM, as described Harshvardhan et al. (1989) and Randall et al. (1989;1991). Major modifications to the original code include an improved cumulus parameterization (Randall and Pan 1993), the inclusion of an updated version of the Simple Biosphere Model as described by Sellers et al. (1995) and a new parameterization of cloud microphysics which is designed to simulate the formation and dissipation of stratiform clouds and precipitation (Fowler et al., 1995; Fowler and Randall 1995). The GCM is a 17-level grid-point model with a horizontal resolution of 4° in latitude by 5° in longitude. The vertical discretization is based on a modified σ-coordinate in which the PBL is the bottom layer of the model. For a further description of the model, see Randall et al. (1991).

A two- month run with downdrafts, called "CUPDW," was carried out starting from a 31 May initial condition obtained from a previous long-term climate simulation performed without cumulus downdrafts. Sea-surface temperatures were prescribed to follow the observed seasonally varying climatology. We have analyzed the second month of the run, i.e. the July results, and have compared with the July results from a corresponding run without downdrafts, called "CONTROL," as well as with observations. CUPDW does not include momentum transport by the downdrafts. Later we show results from a third run, which includes downdraft momentum transport, as a separate sensitivity study.

6. Simulation results

In this section, we first present a few selected quantities which are directly relevant to the cumulus parameterization, in order to show the differences between the updraft-only and updraft-downdraft parameterizations. We then discuss differences of zonal mean cloudiness and the global distribution of PBL properties. This is followed by a discussion of the differences in the atmospheric circulation. Finally, we discuss the effects of downdrafts on the simulated surface energy budget.

6.1 Cumulus effects

We begin our discussion of the results by examining several measures of cumulus activity. Figure 1 presents the global map of cumulus incidence (i.e. frequency of occurrence) simulated with CUPDW, as well as the difference between CUPDW and CONTROL. High values (> 0.5) occur along the ITCZ in both the CONTROL and CUPDW. In most regions of active convection, cumulus convection occurs somewhat more frequently in CUPDW, and the globally averaged cumulus incidence increases in CUPDW. Examples are Central America, the Indian summer monsoon region, and the tropical Western Pacific. CUPDW produces a reduced cumulus incidence over eastern Asia and portions of the North Pacific, however.

The zonally averaged cumulus detrainment mass flux is shown in Fig. 2. This shows the rate at which updrafts detrain. In the Arakawa-Schubert cumulus parameterization, it is assumed that cumulus clouds detrain only at their tops. In effect, then, Fig. 2 shows where the cumulus clouds have their tops. The units are inverse time. This time scale can be interpreted as the time for detrainment to replace all of the air in a layer. Deep convection is intense over the northern tropics (Fig. 2a), and extends with diminished intensity into the middle latitudes of the Northern Hemisphere. Fig. 2b shows a big difference between CONTROL and CUPDW. Deep cumulus convection intensifies in CUPDW in both the tropics and the middle latitudes of the Southern Hemisphere.

As mentioned earlier, we have assumed following Johnson (1976) that the ratio of convective downdraft mass flux and convective updraft mass flux is 0.2. At the lower levels, the updraft and downdraft effects tend to compensate each other; in effect the downdrafts make it more difficult for the updrafts to have their way, e.g. to dry the atmosphere. This may be the reason that we obtained an increased updraft mass flux in CUPDW.

We do not see, in Fig. 2, any tendency for an increased mass flux associated with shallow cumuli. In this respect, our results differ from those of Arakawa and Cheng (1990). We note that Arakawa and Cheng did not assume any fixed relationship between the updraft and downdraft mass fluxes. This may explain why our results differ from theirs.

Fig. 3 a shows the zonally averaged July mean cumulus heating rates taken from the CUPDW. The strongest cumulus heating occurs slightly north of the Equator with a local maximum near 400 mb. Fig.3 b shows the difference in cumulus heating between CUPDW and CONTROL. In general, the cumulus heating is shallower and weaker in CUPDW than in CONTROL especially in the lower tropical troposphere. This result is expected from previous studies of the effects of downdrafts.

Fig.4 shows vertical cross section of the zonally averaged cumulus moistening rate simulated with CUPDW, as well as the differences between CUPDW and CONTROL. Of course, cumuli mainly dry the atmosphere, so many of the values plotted are negative. We do see moistening aloft, however, associated with detrainment of moist air from the clouds. The distributions of the cumulus drying rates in the two simulations are very similar, except that the drying rate is slightly weaker throughout the entire cloud layer in CUPDW than in CONTROL, and is stronger below the cloud layer in CUPDW than in CONTROL. These results are in line with our expectations, based on previous studies reviewed earlier in this paper.

Figure 5 a shows the simulated July-mean cumulus precipitation from CUPDW. There are three distinct local precipitation maxima over the equatorial region near 90°W, and 90°E, respectively. The difference plot between CUPDW and CONTROL is shown in Fig.5 b. Generally, CUPDW generates less cumulus precipitation than CONTROL over the tropics, especially over east Asia and the Western Pacific ocean. This is to be expected, of course, given the reduced convective drying rates discussed above. CUPDW produces a significant increase in precipitation over Central America and the Indian summer monsoon region, however. Comparing Fig.1 b with Fig.5 b, we see that the patterns are similar except in the Western Pacific where the cumulus incidence increases in CUPDW while the cumulus precipitation rate decreases. This suggests that evaporation within the convective downdrafts prevails in those areas, so that more frequent convection results in less precipitation.

From previous experience with the CSU GCM, we are aware that the updraft-only parameterization tends to generate excessive cumulus precipitation over the tropical continents, and that the simulated tropical troposphere is too warm and dry. From the results discussed above, however, we conclude that the convective downdrafts tend to cool and moisten the cloud layer. Similar GCM simulation results were obtained by Sud (1993) and Cheng (1989). The cooling and moistening effects of the downdrafts come from the reduction of the compensating subsidence associated with the total cumulus mass flux, which is due to the downdraft mass flux partially offsetting the updraft mass flux. Our results also show that convective downdrafts cool and dry the subcloud layer. This finding is consistent with those of Gray (1973), Cho and Ogura (1974), Nitta (1975), Molinari and Corsetti (1985) and Sud (1993). Since convective downdrafts are maintained by the evaporation of rain water within updrafts and tend to dry the subcloud layer, it is to be expected that CUPDW will generate less cumulus precipitation than CONTROL. The cooling and moistening due to the downdrafts are strongest near cloud base. Thus, the combined cooling and moistening effects of downdrafts act to destabilize the low-level environment. From this point of view, strong downdraft activity, such as that found in the Indian summer monsoon area and the Western Pacific, favors persistent convection and tends to increase the cumulus incidence over those areas. Furthermore, the widespread increase of the cumulus incidence in CUPDW also helps to destabilize the convective layer through longwave radiative cooling at the cloud tops.

6.2 PBL properties

In this subsection, we select several fields to demonstrate the effects of convective downdrafts on the properties of the PBL.

Figure 6 is a scatter diagram in which the abscissa is the cumulus precipitation rate simulated in CUPDW, and the ordinate is the *change* in PBL depth (Fig. 6 a) or the *change* in PBL mixing ratio (Fig. 6 b) between CUPDW and CONTROL. As discussed earlier the direct effects of convective downdrafts are to deepen and dry the PBL. We have already seen that convection dries the lower troposphere more strongly in CUPDW. Fig. 6 shows, however, that the PBL tends to be both shallower and more moist when cumulus convection is active. The increased updraft mass flux in CUPDW, shown in Fig. 2, can explain these paradoxical results.

Figure 7 shows global maps of the relative humidity at the PBL top as simulated by CONTROL and CUPDW, and the difference. There is very little systematic change due to CUPDW.

Figure 8 shows the global distribution of boundary-layer cloud depth simulated by CUPDW, as well as the difference between CUPDW and CONTROL. Deep boundary-layer clouds (>20 mb) are simulated in the East Pacific and in the middle latitude baroclinic zone of the Southern Hemisphere. The difference field shows that CUPDW creates more shallow clouds in the Eastern Pacific Ocean, Indian summer monsoon area and SPCZ.

The global distribution of PBL wind speed is shown in Fig. 9. Strong winds occur in the Arabian Sea (due to the Indian summer monsoon) and in the middle latitude convergence zone over of the Southern Hemisphere. The difference plot shows that the wind speed generally decreases in the heavy precipitation regions.

6.3 Atmospheric general circulation

In this subsection, we compare a few characteristic components of the atmospheric general circulation as simulated in CUPDW and CONTROL.

The latitude-pressure cross sections of the stream function of the mean meridional circulations obtained with CONTROL and CUPDW look very similar (not shown). However, CUPDW produces a slightly stronger mean meridional circulation than CONTROL, and is in better agreement with ECMWF analyses (not shown). The increased intensity of the mean meridional circulation is consistent with our earlier conclusion that CUPDW leads to more tropical cumulus convection.

Figure 10 a shows the zonally averaged July-mean temperature from CUPDW. The temperature difference between CUPDW and CONTROL is shown in Fig.10 b. In general, CUPDW is cooler than CONTROL, except in the middle latitudes of the Northern Hemisphere, the lower tropical troposphere, and the high latitudes of the Southern Hemisphere. The maximum temperature difference is located near 800 mb in the tropics and near 300 mb in the subtropics. The warmer midlatitudes of the Northern Hemisphere result from increased net radiative heating in CUPDW (not shown).

The CUPDW-simulated zonally averaged distributions of the July-mean specific humidity are shown in Fig.11 a, and the difference between CUPDW and CONTROL is shown in Fig.11 b. Except for the tropical lower atmosphere and near the poles, CUPDW is more moist than CONTROL, especially in the lower tropical troposphere of the Northern Hemisphere.

Naturally, the zonal wind is influenced by the temperature changes discussed above. Fig. 12 shows the zonally averaged zonal wind in CUPDW, as well as the difference between CUPDW and CONTROL. CUPDW weakens the tropical easterlies except near the tropopause; and it also enhances the subtropical westerly jets in both hemispheres, shifting them northward.

In Fig. 13, we compare the global distributions of the monthly-averaged total precipitation simulated in CONTROL against climate data (from Legates and Willmott,1990). The simulated total precipitation map for CUPDW and the difference between CUPDW and CONTROL are shown in Fig. 14. At low latitudes, regions of heavy rainfall are also regions of intense convective activity: along the ITCZ, especially over the Pacific Ocean, over the continents and for the whole monsoon region across the Indian and Western Pacific Oceans. Some of the significant deficiencies of rainfall simulations with CONTROL are seen in Fig. 13 c: (i) excessively strong and steady rainfall over the tropical Western Pacific and SPCZ; and (ii) excessively weak precipitation along the ITCZ. The inclusion of convective downdrafts yields significant differences in the regional distribution and magnitude of the total precipitation, especially in the tropics (Fig. 14). The most striking difference is the increase in total precipitation over the Indian summer monsoon region (particularly the Tibetan Plateau) and tropical East Africa. Over the western Pacific, the rainfall decreases on the eastern side and increases on the western side. Comparing Fig.5 b against Fig. 14 b, we see that the increase in total precipitation results entirely from increased cumulus precipitation over the whole monsoon area. Over deep tropical convective activity centers, the increased cumulus precipitation obtained in CUPDW is in accordance with the decreased cumulus drying rates seen in Fig.4.

6.4 *Surface energy budget*

In view of the large differences in the distributions of temperature and cloudiness, we expect to see significant differences in the distributions of the surface radiation as well. Also, we expect the downdrafts to tend to increase the surface sensible and latent heat fluxes.

Maps of the July-mean surface net longwave radiation (positive upward) for CUPDW, and the corresponding difference fields, are shown in Fig. 15. There is a very sharp contrast in the magnitude of longwave radiation between overcast and cloud free regions (Fig. 15 a). A broad area of high (> 120 W m^{-2}) net longwave radiation stretches across parts of western Africa, India to Central Asia, and the subtropics of the Southern Hemisphere. The heavy rainfall regions, i.e. Central America, Equatorial Africa, and Southeast Asia, are characterized by long wave fluxes less than 90 W m^{-2}. Over these areas, weak net surface longwave cooling results from the downward infrared emission by PBL clouds and water vapor, which compensate much of the upward infrared emission from the surface. Comparison of Fig. 9 b and Fig. 15 b shows that CUPDW yields decreased net surface longwave cooling where PBL cloud amounts are increased, such as the subtropical highs over the continents, and the Indian summer monsoon region. The intensity of the monsoon rainfall (Fig. 14) is strongly increased, so that convective downdrafts tend to generate more shallow clouds and water vapor over that region, and lead to a strong decrease in the regional net infrared emission.

The July-mean surface net shortwave radiation is shown in Fig. 16 for CUPDW and difference fields between CUPDW and CONTROL. Again, CUPDW receives less shortwave radiation over the heavy precipitation areas, since the total cloud amount is increased there.

The surface sensible heat fluxes are displayed in Fig. 17. Strong sensible heat fluxes are found in the major desert regions over the continents. As expected, CUPDW increases the surface sensible heat fluxes over the major convective areas, such as east Asia, by cooling the boundary layer. This effect is fairly weak, however. Since shallow clouds act to cool the surface by restricting incoming insolation, we expect to see a decrease of the surface sensible heat flux in the continental regions where low-level cloud amount is increased.

The final component of the surface energy budget is the surface latent heat flux, which is shown in Fig. 18. Since CUPDW tends to dry the lower troposphere, the latent heat fluxes are generally increased in CUPDW. The main differences between CONTROL and CUPDW are: CUPDW enhances the latent heat fluxes in the subtropics of the Southern Hemisphere, and the India monsoon area, especially in the Arabian Sea.

Fig. 19 shows zonally averaged distributions of the *differences* of the monthly averaged net downward surface energy flux, surface net longwave radiative flux, surface shortwave radiative flux, surface latent heat flux and surface sensible heat flux between CUPDW and CONTROL. In the tropics, downdrafts have little effect on the net downward surface energy flux. The latent heat flux and net downward surface shortwave flux do show some differences between the two runs, however. In the subtropics of the Northern Hemisphere, CUPDW decreases the surface longwave flux (6 W m^{-2}), the shortwave flux (8 W m^{-2}) and the sensible heat flux (3 W m^{-2}), with an increase of the latent heat flux (5 W m^{-2}). In contrast, an increase of longwave and shortwave radiative fluxes (3 W m^{-2}), and the sensible heat flux (1 W m^{-2}), and a decrease of the latent heat flux (6 W m^{-2}) occur in the winter hemisphere.

6.5 Sensitivity to α

We performed a sensitivity test to see how our results depend on the assumption that the updraft and downdraft mass fluxes are in constant ratio α. Fig. 20 shows the cumulus heating and moistening rates simulated in an experiment with $\alpha = 0.4$; recall that in CUPDW we used $\alpha = 0.2$. Comparing Fig.20 with Fig.3 a and Fig.4 a, we see that the results obtained with the downdraft parameterization are very sensitive to the value of α. This conclusion is not unexpected; it indicates the need for a more sophisticated parameterization in which the downdraft mass flux is determined through a physically based closure assumption, as in Cheng (1989).

6.6 *The effects of downdraft momentum transports*

Ours is the first GCM study of the effects of downdraft momentum transports on the atmospheric general circulation. Fig. 21 a shows the difference field of latitude-pressure cross sections of the zonally averaged zonal wind, between CUPDW and ECMWF. The difference plot between EXP3 (CUPDW with momentum transport by convective downdrafts) and CUPDW is shown in Fig. 21 b. This figure reveals that downdraft momentum transports weaken the westerly jets, which are too strong in CUPDW. We also see that the westerly belt north of Antarctica is strengthened; this is an improvement in the simulation.

Fig. 22 is a scatter diagram in which the abscissa is the cumulus precipitation rate simulated in CUPDW, and the ordinate is the *change* in PBL wind speed (Fig.22 a) or the *change* in surface latent heat flux (Fig.22 b) between EXP3 and CUPDW. We see that EXP3 tends to increase PBL wind speed when the cumulus convection is active, and that the surface latent heat flux is stronger in EXP3 than in CUPDW when cumulus convection is active.

6.7 *Discussion*

Comparisons between simulations with the updraft-only parameterization and with the updraft-downdraft parameterization shows that convective downdrafts can produce: 1) cooling and moistening of the free atmosphere; and 2) a better simulation of temperature, humidity, and precipitation over the warm pool region of the tropical Western Pacific. These findings are consistent with those of Cheng and Arakawa (1990), and Sud and Walker (1993). Our results also show that downdrafts tend to enhance convective instability and generate more low-level stratiform clouds by moistening and cooling the lower cloud layer. Downdrafts also tend to dry the boundary layer, by injecting dry air. In strongly convective regions, convective downdrafts increase the surface sensible and latent heat fluxes (as also found by Sud and Walker, 1993).

Finally, downdraft momentum transports tend to increase the wind speed near the surface in convectively active regions.

7. Summary and conclusions

From previous experience with the CSU GCM, we are aware that some of the outstanding deficiencies of tropical circulation and rainfall simulations with updraft-only A-S parameterization are: (1) excessively strong and steady rainfall over the tropical Western Pacific (2) an excessively warm PBL with a weakly negative sensible heat flux over the tropical ocean; (3) the inability of the summer monsoon to extend northward over the Himalayan Mountains.

Clearly, rainfall and drying without rain evaporation and downdrafts would produce excessive warming of the air column, which would in turn produce a positive feedback by lowering the surface pressure and promoting low-level convergence, rising motion, and precipitation, particularly in the tropics where the circulation is thermally driven. This suggests that downdrafts might alleviate some of the problems of the standard version of the model.

We have followed Johnson's approach to construct an updraft-downdraft cumulus ensemble model as an extension of the prognostic Arakawa-Schubert cumulus parameterization. We tested the combined updraft-downdraft model in a 2-month simulation with the CSU GCM. The results show that convective downdrafts can produce: 1) cooling and drying of the boundary layer, together with cooling and moistening of the free atmosphere; and 2) a better simulation of temperature, humidity, and precipitation over the warm pool region of the tropical Western Pacific. These findings are consistent with those of Cheng and Arakawa (1990), and Sud and Walker (1993).

The changes in the surface energy budget and the general circulation are the most significant differences between the GCM experiments with and without the effects of convective downdrafts. Comparisons between CONTROL and CUPDW show that the diabatic forcing of the tropospheric large-scale flow is more realistic with the downdrafts. We also found that downdrafts tend to moisten and cool the lower troposphere, thus generating more shallow stratiform clouds. Analysis of the surface fluxes indicates that convective downdrafts particularly change the surface latent heat flux, and also the surface shortwave radiation through the changes in convectively induced cloud cover and precipitation.

The sensitivity test on α, the ratio of updrafts mass flux and downdrafts mass fluxes, shows that the results from CUPDW are very sensitive to the assumed value of α.

In the GCM simulations with momentum transport by convective downdrafts, downdrafts transports of momentum do increase PBL wind speed which, in term, increase the cumulus incidence and surface heat fluxes over active cumulus regions in EXP3.

The results of this paper clearly demonstrate that moisture-cloudiness-radiation processes are important for the simulation of climate. It would be of interest to make comparisons on the variations of diurnal and seasonal cycle between the simulations made with CONTROL and CUPDW. Further development of an interactive cumulus-PBL parameterization is required to study the interactions of cumulus convection and the PBL, and the effects of these interactions on the global circulation of the atmosphere.

In view of the effects of downdrafts on the general circulation, a more detailed approach to their parameterization, such as that followed by Cheng and Arakawa (1990), is clearly needed for the future.

Acknowledgments

This research was sponsored by the National Science Foundation under grants ATM-9121629 and ATM-9214981, and by the U.S. Department of Energy under grant DE-FG03-94ER91629. Computing resources were provided by the Scientific Computing Division at the National Center for Atmospheric Research, by the National Center for Computational Sciences at NASA/Goddard, and by the National Energy Research Computer Center at Lawrence Livermore National Laboratory.

Appendix

The Updraft-Downdraft Cumulus Ensemble Model

This appendix describes in detail the procedure for diagnosing cloud properties from a given large-scale environment. The updraft-only version of this model is identical to the one-dimension cumulus ensemble model used by Randall and Pan (1993), who followed Arakawa and Schubert (1974). Convective-scale precipitation-driven downdrafts are parameterized following the method proposed by Johnson (1976). The following is a brief description of the updraft-downdraft cumulus ensemble model used in this study.

A.1 Formulations

A.1.1 Mass budget of the clouds

Fig.23 illustrates the fundamental features of this updraft-downdraft model. It is assumed that each updraft has an accompanying downdraft and that both have the same fractional mass entrainment rate, λ. Following Arakawa and Schubert (1974), the thermodynamic profile of an updraft subensemble, which has a constant fractional rate of entrainment, is uniquely defined under given large-scale conditions if the buoyancy condition at the cloud top is specified. Thus, the mass budget equation for each updraft can be written as

$$\frac{1}{m_u(z,\lambda)}\frac{\partial}{\partial z}m_u(z,\lambda) = \lambda, \qquad \text{(A.1)}$$

where $m_u(z,\lambda)$ is the mass flux of cloud updrafts (subscript u) with entrainment rate λ. Solving (A.1), we have $m_u(z,\lambda) = m_B(\lambda)\,exp\{\lambda[z - z_B(\lambda)]\}$,where $m_B(\lambda)$ is the

cloud base mass flux distribution function and $z_B(\lambda)$ is the height of the cloud base. For convenience, we introduce a normalized mass flux

$$\eta_u(z, \lambda) = \frac{m_u}{m_B} = exp\int_{z_b}^{z} \lambda dz. \tag{A.2}$$

The mass budget per unit of cloud-base mass flux for updraft can be written as

$$\frac{1}{\eta_u(z, \lambda)} \frac{\partial}{\partial z} \eta_u(z, \lambda) = \lambda. \tag{A.3}$$

Since we model downdraft as inverted plumes, the mass budget equation of downdrafts can be written as

$$\frac{1}{\eta_d(z, \lambda)} \frac{\partial}{\partial z} \eta_d(z, \lambda) = -\lambda, \tag{A.4}$$

where $\eta_d(z, \lambda)$ is the mass flux of cloud downdrafts (subscript *d*) with entrainment rate λ. For each cloud

$$\eta_d(z, \lambda) = \eta_0(\lambda) \, exp\{\lambda[z_0(\lambda) - z]\}, \tag{A.5}$$

where $\eta_0(\lambda)$ is the downdraft-originating-level mass flux distribution function and $z_0(\lambda)$ is the downdraft originating level. This level probably exists somewhere between mid-cloud and cloud-top. As indicated, it is a function of the entrainment rate λ, i.e., of the cloud type. As suggested by Johnson (1976), we assume for simplicity that it is only when the downdraft reaches the level z_0 that it takes on a plume-like behavior with an increase in mass flux given by (A.5). It is assumed that the downdraft motion above z_0 contributes negligibly to the total convective mass flux.

A.1.2 Moist static energy budget of the clouds

Assuming that radiative heating plays only a minor role in the growth of individual cumulus clouds, the budgets of moist static energy for the subensemble in steady state are given by:

$$\frac{\partial}{\partial z}[m_u(z,\lambda)\,h_u(z,\lambda)] = \bar{h}\frac{\partial}{\partial z}[m_u(z,\lambda)], \tag{A.6}$$

$$\frac{\partial}{\partial z}[m_d(z,\lambda)\,h_d(z,\lambda)] = \bar{h}\frac{\partial}{\partial z}[m_d(z,\lambda)], \tag{A.7}$$

for the updraft and downdraft, respectively. The moist static energy $h_u(z,\lambda)$ within each cumulus updraft is given by integrating (A.6) from cloud base $z_b(\lambda)$ to the level z:

$$h_u(z,\lambda) = \frac{1}{\eta_u(z,\lambda)}\left[h_u(z_b,\lambda) + \int_{z_b}^{z}\lambda\eta_u(z',\lambda)\,\bar{h}(z')\,dz'\right]. \tag{A.8}$$

The moist static energy within the downdraft is given by the solution to (A.7), i.e., by

$$h_d(z,\lambda) = \frac{1}{\eta_d(z,\lambda)}\left[h_d(z_0,\lambda) + \int_{z}^{z_0}\lambda\eta_d(z',\lambda)\,\bar{h}(z')\,dz'\right]. \tag{A.9}$$

A.1.3 Moisture budget of the clouds

In the entrainment layer of the ith cloud, the budget equations for total water, for updraft and downdraft, can be written as

$$\frac{\partial}{\partial z}[\eta_u(z,\lambda)\,q_u(z,\lambda)] = \bar{q}\frac{\partial}{\partial z}(\eta_u(z,\lambda)) + c(z,\lambda), \tag{A.10}$$

and

$$\frac{\partial}{\partial z}[\eta_d(z,\lambda)\,q_d(z,\lambda)] = \bar{q}\frac{\partial}{\partial z}(\eta_d(z,\lambda)) - e_d(z,\lambda), \tag{A.11}$$

respectively, where c denotes the condensation rate within convective updrafts, and e_d represents the evaporation rate in the convective downdrafts.

A.1.4 Momentum budget of the clouds

Assuming that momentum inside the updrafts and downdrafts varies with height only as a result of entrainment, the budgets of momentum for each sub-ensemble in steady state are given by

$$\frac{\partial}{\partial z}[m_u(z,\lambda)\,U_u(z,\lambda)] = \bar{U}\frac{\partial}{\partial z}([m_u(z,\lambda)]), \tag{A.12}$$

and

$$\frac{\partial}{\partial z}[m_d(z,\lambda)\,U_d(z,\lambda)] = \bar{U}\frac{\partial}{\partial z}[m_d(z,\lambda)], \tag{A.13}$$

for the updraft and downdraft, respectively.

A.1.5 Large-scale budgets

We assume that cumulus clouds modify the environment through the detrainment of energy and water substance and through the vertical mass flux of the environment which compensates the mass flux of cumulus clouds (Oyama 1971; Yanai et al. 1973; Arakawa and Schubert 1974). The large-scale heating and drying rates due to the *i*th cumulus subensemble are given by

$$\left(\frac{\partial\bar{T}}{\partial t}\right)_{cu} = \frac{1}{C_p}\left(\frac{\partial\bar{h}}{\partial t}\right)_{cu} - L\left(\frac{\partial\bar{q}}{\partial t}\right)_{cu}, \tag{A.14}$$

$$\left(\frac{\partial\bar{h}}{\partial t}\right)_{cu} = \delta_u(h_u - \bar{h}) - m_u\frac{\partial\bar{h}}{\partial p} - m_d\frac{\partial\bar{h}}{\partial p}, \tag{A.15}$$

$$\left(\frac{\partial\bar{q}}{\partial t}\right)_{cu} = \delta_u(q_u - \bar{q} + l) - m_u\frac{\partial\bar{q}}{\partial p} - m_d\frac{\partial\bar{q}}{\partial p}, \tag{A.16}$$

where δ is the rate of mass detrainment per unit pressure interval. The conservations of the moist static energy and water substance require

$$\int_{p(i)}^{p(N+\frac{1}{2})} \left(\frac{\partial \bar{h}}{\partial t}\right)_{cu} dp = 0, \tag{A.17}$$

and

$$-\int_{p(i)}^{p(N+\frac{1}{2})} \left(\frac{\partial \bar{q}}{\partial t}\right)_{cu} dp = R, \tag{A.18}$$

where R is the rate of rainwater generation per unit m_B.

The effects on the large-scale momentum fields, due to the ith of cumulus subensemble are given as

$$\left(\frac{\partial \bar{\boldsymbol{U}}}{\partial t}\right)_{cu} = \delta_u (\boldsymbol{U}_u - \bar{\boldsymbol{U}}) - m_u \frac{\partial \bar{\boldsymbol{U}}}{\partial p} - m_d \frac{\partial \bar{\boldsymbol{U}}}{\partial p} \tag{A.19}$$

A.1.6 Thermodynamic budgets of the PBL

In the CSU GCM, the PBL is assumed to be well-mixed above the surface layer, and to be capped by discontinuities in temperature, moisture and wind velocity. The PBL interacts with the free atmosphere through cumulus convection and by turbulent entrainment at the PBL top. Following Suarez et al. (1983), the mass, thermodynamic, and momentum budgets of the PBL can be written as:

$$\frac{\partial (\delta p)}{\partial t} = -\nabla \bullet (\delta p \boldsymbol{U}_M) + g (E - M_B - \Sigma m_{d,B}) \tag{A.20}$$

$$\frac{\partial}{\partial t}[\pi h_M + \nabla \bullet (\pi U_M h_M)] = g[Eh_{B+} - M_B h_M - \Sigma m_{d,B} h_d] + S_h, \tag{A.21}$$

$$\frac{\partial}{\partial t}[\pi q_M + \nabla \bullet (\pi U_M q_M)] = g[Eq_{B-} - M_B q_M - \Sigma m_{d,B} q_d] + S_q, \tag{A.22}$$

$$\frac{\partial}{\partial t}[\pi \boldsymbol{U}_M + \nabla \bullet (\pi \boldsymbol{U}_M)] = g[E\boldsymbol{U}_{B+} - M_B \boldsymbol{U}_M - \Sigma m_{d,B} U_d] + S_m \tag{A.23}$$

where E is the PBL top entrainment, subscript B^+ denotes the level just above the transition zone, and subscript M denotes a vertical mean through the PBL. $S_{h,}$ S_q and S_m are the surface fluxes and radiation terms. π is the pressure depth of the PBL, and **U** is the horizontal velocity.

A.2 Discrete Model

A.2.1 Mass Budget

We follow the discrete model as implemented by Lord et al. (1982) who decomposed the cloud ensemble into sub-ensembles according to the cloud-top level, rather than the fractional entrainment rate. As shown in the Fig. 24, the vertical structure of the ith cloud type, the cloud tops are defined at the integer levels, and a cloud which has its top at level i, where $1 \le i \le KF$ and KF is the index of the layer immediately above the sub-cloud layer, is defined as the ith cloud type. The ith cloud type is assumed to be representative of the cloud sub-ensemble with tops in layer i. The fractional entrainment rate of the ith cloud type is defined by λ, and the cloud-top pressure is denoted by $\hat{p}(i)$ .Using this approach, the discrete form of (A.3) can be written as

$$\eta_u\left(k-\frac{1}{2}, i\right) = \eta_u\left(k+\frac{1}{2}, i\right)[1+\lambda(i)\Delta z(k)], \tag{A.24}$$

here $\Delta z(k) = z(k-\frac{1}{2}) - z(k+\frac{1}{2})$, and $\eta_u(N-\frac{1}{2}, i) = 1$. The mass budget for the cloud-top layer $k=i$ is given by

$$\eta_u(i, i) = \eta_u(i+\frac{1}{2}, i)\ [1+\lambda(i)\,\hat{\Delta}z(k)], \tag{A.25}$$

where $\hat{\Delta}z(i) = z(i) - z(i+\frac{1}{2})$.

Similarly, the mass budget for the downdraft, (A.5), can be written as

$$\eta_d(k+\frac{1}{2}, i) = \eta_d(k-\frac{1}{2}, i)\ [1+\lambda(i)\,\Delta z(k)] \tag{A.26}$$

At the downdraft starting level, layer k_0, (A.26) is

$$\eta_d(k_0+\frac{1}{2}, i) = \eta_d(k_0, i)\ [1+\lambda(i)\,\hat{\Delta}z(k_0)], \tag{A.27}$$

and $\eta_d(k_0, i) = 1$.

We assume that the downdrafts originate at a level above cloud base and below cloud top, given by a certain fraction β of the pressure-depth of the corresponding updraft. A relation between the downdraft-origination-level mass flux $M_0(\lambda)$ and the updraft-cloud-base mass flux $M_B(\lambda)$, $\frac{M_0(\lambda)}{M_B(\lambda)} = -\varepsilon(\lambda)$, was used. We follow Johnson (1976) by choosing $\beta = 0.75$ and $\varepsilon(\lambda) = 0.2$.

A.2.2 Moist Static Energy Budget

For layer k and cloud type i, we let $h_u(k+\frac{1}{2}, i)$ be the subensemble moist static energy before entrainment, and $h_u(k-\frac{1}{2}, i)$ be the subensemble moist static energy after entrainment for the updrafts. Then the discrete form of (A.8) is

$$h_u(k-\frac{1}{2}, i) = \frac{h_u(k+\frac{1}{2}, i) + \lambda(i)\,\Delta z(k)\,\bar{h}(k)}{1+\lambda(i)\,\Delta z(k)}. \tag{A.28}$$

When $k=KF$ (the lowest level in the model) in (A.28), $h_u(KF+\frac{1}{2}, i) = h_m$. Here h_m is the moist static energy of the sub-cloud layer. For the cloud-top detrainment layer, (A.28) becomes

$$\hat{h}_u(i, i) = \frac{h_u(i+\frac{1}{2}, i) + \lambda(i)\,\hat{\Delta z}(i)\,\bar{h}(i)}{1+\lambda(i)\,\hat{\Delta z}(i)}, \tag{A.29}$$

where $\hat{h}_u(i, i)$ is the moist static energy of cloud type i at the cloud-top.

Similarly, the moist static energy budget for the downdraft can be written as

$$h_d(k+\frac{1}{2}, i) = \frac{h_d(k-\frac{1}{2}, i) + \lambda(i)\,\Delta z(k)\,\bar{h}(k)}{1+\lambda(i)\,\Delta z(k)}. \tag{A.30}$$

At the downdraft starting level, layer k_0, (A.30) is

$$h_d(k_0+\frac{1}{2}, i) = \frac{h_{d0}(k_0, i) + \lambda(i)\,\hat{\Delta z}(k_0)\,\bar{h}(k_0)}{1+\lambda(i)\,\hat{\Delta z}(k_0)}. \tag{A.31}$$

We select $h_{d0}(k_0, i) = \bar{h}^*(k_0)$, following Johnson(1976), where $h^* = s + Lq^*$ is the saturation moist static energy.

A.2.3 Water Vapor Budget

The budget for total cloud water is calculated in two steps as described below. Let $q(k+\frac{1}{2}, i)$ be the value entering layer k from below, $q(k, i)$ the value after entrainment but before the precipitation process, and $q(k-\frac{1}{2}, i)$ the value after the precipitation process. The latter is also the value leaving layer k. Also, let $q_l(k, i)$ be the cloud suspended liquid water mixing ratio before precipitation process has been completed.

From (A.10) and the definition of $q(k, i)$, we can show that

$$q(k, i) = \frac{q(k+\frac{1}{2}, i) + \lambda(i)\Delta z(k)\bar{q}(k)}{1+\lambda(i)\Delta z(k)}, \tag{A.32}$$

where $\bar{q}(k)$ is the large-scale total water mixing ratio and is identical to $\bar{q}_v(k)$ when the environment is not supersaturated. When k=KF in (A.32), $q(KF+\frac{1}{2}, i) = q_{vm}$. Here q_{vm} is the water vapor mixing ratio of the sub-cloud layer, and is calculated as the average of the sub-cloud layer water vapor mixing ratio in the present model.

The second step is to determine the amount of precipitation produced in layer k from cloud type i. When the cloud is saturated at level k the cloud water vapor mixing ratio is calculated from

$$q_v(k, i) = \bar{q}_v(k) + \frac{\gamma(k)}{L[1+\gamma(k)]}\left[h(k-\frac{1}{2}, i) - \bar{h}^*(k)\right], \tag{A.33}$$

where $\gamma(k) = \frac{L}{C_p}\left[\frac{\partial \bar{q}_v^{*}(k)}{\partial T}\right]_p$. Then the resulting suspended liquid water mixing ratio before precipitation is $q_l(k, i) = q(k, i) - q_v(k, i)$. Part of $q_l(k, i)$ is converted into precipitation by assuming a constant conversion rate per unit height, $C_0 = 2 \times 10^{-3} m^{-1}$, following Lord (1982). Therefore, the liquid water mixing ratio after precipitation in the layer k, for cloud type i, is

$$q_l\left(k-\frac{1}{2}, i\right) = q_l(k, i) - c_0 \Delta z(k)\, q_l\left(k-\frac{1}{2}, i\right), \tag{A.34}$$

from which we get

$$q_l\left(k-\frac{1}{2}, i\right) = \frac{q_l(k, i)}{1 + c_0 \Delta z(k)}. \tag{A.35}$$

The total cloud water mixing ratio leaving layer k is

$$q\left(k-\frac{1}{2}, i\right) = q(k, i) - c_0 \Delta z(k)\, q_l\left(k-\frac{1}{2}, i\right). \tag{A.36}$$

The water vapor mixing ratio of the downdraft is controlled by both the entrainment of environment air and the re-evaporation of the precipitation within the downdraft. The influence of the re-evaporation will be discussed later when we calculate the final precipitation rate. Here we only consider the effects of entrainment on the budget of the downdraft water vapor mixing ratio. Let $q_d\left(k-\frac{1}{2}, i\right)$ be the downdraft water vapor mixing ratio for cloud type i before entering layer k from above, and $q_d\left(k+\frac{1}{2}, i\right)$ be the one leaving layer k after the entrainment. Then

$$q_d\left(k+\frac{1}{2}, i\right) = \frac{q_d\left(k-\frac{1}{2}, i\right) + \lambda(i)\, \Delta z(k)\, \bar{q}(k)}{1 + \lambda(i)\, \Delta z(k)}. \tag{A.37}$$

At the downdraft starting level, layer k_0, (A.37) is

$$q_d(k_0 + \frac{1}{2}, i) = \frac{q_{d0}(k_0, i) + \lambda(i)\hat{\Delta z}(k_0)\bar{q}(k_0)}{1 + \lambda(i)\hat{\Delta z}(k_0)}. \tag{A.38}$$

Following Johnson (1976), it is reasonable to let $q_{d0}(k_0, i) = \bar{q}^*(k_0)$.

A.2.4 Momentum Budget

The discrete form of (A.12) is

$$\boldsymbol{U}_u(k - \frac{1}{2}, i) = \frac{\boldsymbol{U}_u(k + \frac{1}{2}, i) + \lambda(i)\Delta z(k)\bar{\boldsymbol{U}}(k)}{1 + \lambda(i)\Delta z(k)}. \tag{A.39}$$

When $k=KF$ in (A.39), $\boldsymbol{U}_u(KF + \frac{1}{2}, i) = \bar{\boldsymbol{U}}_M$. Here $\bar{\boldsymbol{U}}_M$is the mean wind of the sub-cloud layer. For the cloud-top detrainment layer, (A.39) becomes

$$\hat{\boldsymbol{U}}_u(i, i) = \frac{\boldsymbol{U}_u(i + \frac{1}{2}, i) + \lambda(i)\hat{\Delta z}(i)\bar{\boldsymbol{U}}(i)}{1 + \lambda(i)\hat{\Delta z}(i)}, \tag{A.40}$$

where $\hat{\boldsymbol{U}}_u(i, i)$ is the moist static energy of cloud type i at the cloud-top.

Similarly, the momentum budget for the downdraft can be written as

$$\boldsymbol{U}_d(k + \frac{1}{2}, i) = \frac{\boldsymbol{U}_d(k - \frac{1}{2}, i) + \lambda(i)\Delta z(k)\bar{\boldsymbol{U}}(k)}{1 + \lambda(i)\Delta z(k)}. \tag{A.41}$$

At the downdraft starting level, layer k_0, (A.41) is

$$\hat{U}_d(k_0+\frac{1}{2},i) = \frac{U_{d0}(k_0,i)+\lambda(i)\hat{\Delta z}(k_0)\overline{U}(k_0)}{1+\lambda(i)\hat{\Delta z}(k_0)}. \tag{A.42}$$

We select $U_{d0}(k_0,i) = \overline{U}(k_0)$.

A.2.5 Large Scale Budgets

The numerical schemes designed for calculating (A.15) and (A.16) should satisfy the constraints (A.17) and (A.18). Following Cheng (1989), the discrete forms of (A.15) and (A.16) are

$$\begin{aligned}\int_{p(k-\frac{1}{2})}^{p(k+\frac{1}{2})}\frac{1}{m_B}\left(\frac{\partial\bar{h}}{\partial t}\right)_u dp &= -\eta_u(k-\frac{1}{2})\left[h_u(k-\frac{1}{2})-\bar{h}(k-\frac{1}{2})\right] \\ &\quad+\eta_u(k+\frac{1}{2})\left[h_u(k+\frac{1}{2})-\bar{h}(k+\frac{1}{2})\right],\end{aligned} \tag{A.43}$$

and

$$\begin{aligned}\int_{p(k-\frac{1}{2})}^{p(k+\frac{1}{2})}\frac{1}{m_B}\left(\frac{\partial\bar{q}}{\partial t}\right)_u dp &= -\eta_u(k-\frac{1}{2})\left[q_u(k-\frac{1}{2})-\bar{q}(k-\frac{1}{2})\right] \\ &\quad+\eta_u(k+\frac{1}{2})\left[q_u(k+\frac{1}{2})-\bar{q}(k+\frac{1}{2})\right]-R(k).\end{aligned} \tag{A.44}$$

Here $R(k)$ represents the rate of rainwater generation per unit m_B.

Similarly, the discrete form of the effects of downdraft on the large scale budgets can be written as

$$\int_{p(k-\frac{1}{2})}^{p(k+\frac{1}{2})} \frac{1}{m_{d0}} \left(\frac{\partial \bar{h}}{\partial t}\right)_d dp = -\eta_d(k-\frac{1}{2})\left[h_d(k-\frac{1}{2}) - \bar{h}(k-\frac{1}{2})\right], \qquad \text{(A.45)}$$

$$+\eta_d(k+\frac{1}{2})\left[h_d(k+\frac{1}{2}) - \bar{h}(k+\frac{1}{2})\right],$$

$$\int_{p(k-\frac{1}{2})}^{p(k+\frac{1}{2})} \frac{1}{m_{d0}} \left(\frac{\partial \bar{q}}{\partial t}\right)_d dp = -\eta_d(k-\frac{1}{2})\left[q_d(k-\frac{1}{2}) - \bar{q}(k-\frac{1}{2})\right]. \qquad \text{(A.46)}$$

$$+\eta_d(k+\frac{1}{2})\left[q_d(k+\frac{1}{2}) - \bar{q}(k+\frac{1}{2})\right].$$

After obtaining the cloud-base mass flux, $M_B(i)$, for each cloud type i, we can calculate the precipitation rate. In the approach of Lord et al. (1982), the precipitation rate due to the updrafts only is given by

$$P_u = \sum_{i=1}^{i_{max}} \sum_{k=i}^{i_{max}} c_0 \Delta z(k)\, q_l(k-\frac{1}{2}, i)\, \eta_u(k-\frac{1}{2}, i)\, M_B(i). \qquad \text{(A.47)}$$

Here $q_l(k-\frac{1}{2}, i)$ is calculated from (A.35).

The re-evaporation of precipitation within downdrafts, E_d, is calculated as follows. Following Johnson (1976), we assume that the downdrafts are saturated at the cloud-base level. Then, from the definition of moist static energy we can calculate the temperature of downdrafts at the cloud-base level, $T_d(KF+\frac{1}{2}, i)$, by an iteration. Next, the final downdraft water vapor mixing ratio is obtained from $q_d(KF+\frac{1}{2}, i) = q^*\left[T_d(KF+\frac{1}{2}, i)\right]$. From (A.32), we can obtain the modified downdraft water vapor mixing ratio at the cloud-base level only by entrainment effect, $q_{de}(KF+\frac{1}{2}, i)$. Then, E_d, the amount of water vapor coming from the re-evaporation of the precipitation in downdraft, is calculated as:

$$E_d = \sum_{i=1}^{KF} \left[q_d(KF+\frac{1}{2}, i) - q_{de}(KF+\frac{1}{2}, i) \right] \eta_d(KF+\frac{1}{2}, i) M_0(i) \tag{A.48}$$

The total precipitation rate is then given by P_u-E_d.

The momentum transport by updrafts and downdrafts (A.19) can be written as

$$\begin{aligned} \int_{p(k-\frac{1}{2})}^{p(k+\frac{1}{2})} \frac{1}{m_B} \left(\frac{\partial \bar{\mathbf{U}}}{\partial t}\right)_u dp = & -\eta_u(k-\frac{1}{2}) \left[\mathbf{U}_u(k-\frac{1}{2}) - \bar{\mathbf{U}}(k-\frac{1}{2}) \right] \\ & + \eta_u(k+\frac{1}{2}) \left[\mathbf{U}_u(k+\frac{1}{2}) - \bar{\mathbf{U}}(k+\frac{1}{2}) \right] , \end{aligned} \tag{A.49}$$

$$\begin{aligned} \int_{p(k-\frac{1}{2})}^{p(k+\frac{1}{2})} \frac{1}{m_{d0}} \left(\frac{\partial \bar{\mathbf{U}}}{\partial t}\right)_d dp = & -\eta_d(k-\frac{1}{2}) \left[\mathbf{U}_d(k-\frac{1}{2}) - \bar{\mathbf{U}}(k-\frac{1}{2}) \right] \\ & + \eta_d(k+\frac{1}{2}) \left[\mathbf{U}_d(k+\frac{1}{2}) - \bar{\mathbf{U}}(k+\frac{1}{2}) \right] , \end{aligned} \tag{A.50}$$

References

Arakawa, A., and W. Schubert, Interaction of a cumulus cloud ensemble with the large-scale environment, Part I, *J. Atmos. Sci.*, *31*, 674-701, 1974.

Betts, A. K., Thermodynamic transformation of the tropical subcloud layer by precipitation and downdraft, *J. Atmos.* Sci., *33*, 1008-1020, 1976.

_______, Saturation point analysis of moist convective overturning, *J. Atmos. Sci.*, *39*, 1484-1505, 1982.

_______, Boundary layer thermodynamics of a high plains severe storm, *M*on. *Wea.* R*ev*, *112*, 2199-2211, 1984.

_______, and Silva Dias, Unsaturated downdraft in cumulonimbus, *J. Atmos. Sci.*, *36*, 1061-1071, 1979.

_______, A. K. and M. J. Miller, *The Betts-Miller scheme. The representation of cumulus convection in numerical models of the atmospher*e, K. A. Emanuel and D. J. Raymond, Ed., American Meteorological Society, 1993.

Barnes, G. and M. Garstang, Subcloud layer energetics of precipitating convection, *Mon. Wea.* R*ev*, *110*, 102-117, 1982.

Bradley, E. F., C. A. Coppin, and J. S. Godfrey, Measurements of sensible and latent heat flux in the western equatorial Pacific Ocean, *J. Geophys. Res.*, *96*, 3375-3389, 1991.

Brummer, B., Mass and energy budgets of a 1 km high atmospheric box over the GATE C-Scale triangle during undisturbed and disturbed weather conditions, *J. Atmos.* Sci., *35*, 997-1011, 1978.

Byers, H. R., and R. R. Braham, *The Thunderstorm*, U.S. Department of Commerce, 287 pp, 1949.

Charba, J., Application of gravity current model to analysis of squall-line gust front, *Mon. Wea. Rev.*, *102*, 140-156, 1974.

Cheng, M.-D., Effects of downdrafts and mesoscale convective organization on the heat and moisture budgets of tropical cloud clusters. Part I: A diagnostic cumulus ensemble model, *J.Atmos.Sci.*, *46*, 1517-1538, 1989a.

______, Effects of downdrafts and mesoscale convective organization on the heat and moisture budgets of tropical cloud clusters. Part II: Effects of convective-scale downdrafts, *J. Atmos. Sci.*, *46*, 1540-1564, 1989b.

______, and A. Arakawa, Inclusion of convective downdrafts in the Arakawa-Schubert cumulus parameterization, Technical Report, Department of Atmospheric Sciences, UCLA, Los Angeles, CA, 69 pp, 1990.

Cho, H. R., and Y. Ogura, A relationship between the cloud activity and the low-level convergence as observed in Reed-Recker's composite easterly waves, *J. Atmos. Sci.*, *31*, 2058-2065, 1974.

______, and ______, On the interaction between the subcloud and cloud layers in tropical regions, *J. Atmos. Sci.*, *31*, 1850-1857, 1974.

David B. P., The influence of convective outflows on the air-sea interface during TOGA COARE. *Proc. 5th Symposium on Global Change Study, Amer. Meteor. Soc.*, J77-J80, 1994.

Echternacht, K. L., and M. Garstang, Changes in the structure of the tropical sub-cloud layer from the undisturbed to disturbed states, *Mon. Wea. Rev.*, *104*, 407-417, 1976.

Emanuel, K. A., A similarity theory for unsaturated downdrafts within clouds, *J. Atmos. Sci.*, *38*, 1541-1557, 1981.

______, A scheme for representing cumulus convection in large-scale models, *J. Atmos. Sci.*, *48*, 2313-2335, 1991.

Emmitt, G. D., Tropical cumulus interaction with and modification of the sub-cloud region, *J. Atmos. Sci.*, *35*, 1485-1502, 1978.

Fankhauser, J. C., I. R. Paluch, W. A. Cooper, D. W. Breed, and R. E. Rinehart, Air Motion and Thermodynamics, in *Hailstorms of the Central High Plains, Vol. I: The National Hail Research Experiment*, edited by C. Knight and P. Squires, Colo. Assoc. Univ. Press, 134-145, 1982.

Fujita, T. and R. M. Wakimoto, Five scales of airflow associated with a series of downbursts on 16 July 1980, *Mon. Wea. Rev.*, *109*, 1438-1456, 1981.

Fitzjarrald, D. R., and M. Garstang, Vertical structure of the tropical boundary layer, *Mon. Wea. Rev.*, *109*, 1512-1526, 1981a.

_______, and _______, Boundary-layer growth over the tropical ocean, *Mon. Wea. Rev.*, *109*, 1762-1772, 1981b.

Foote, G. B. and H. B. Frank, Case study of a hailstorm in Colorado. Part III: Airflow from triple-Doppler measurements, *J. Atmos. Sci.*, *40*, 686-707, 1983.

Fowler, L. A., D. A. Randall, and S. A. Rutledge, Liquid and ice cloud microphysics in the CSU general circulation model. Part I: Model description and simulated microphysical processes, *J. Clim.* (in press), 1995.

Fowler, L. A. and D. A. Randall, Liquid and ice cloud microphysics in the CSU general circulation model. Part II: Impact on cloudiness, the Earth's radiation budget, and the general circulation of the atmosphere, *J. Clim.* (in press), 1995.

Gaynor, J. E., and P. A. Mandics, Analysis of the tropical marine boundary layer during GATE using acoustic sounder data, *Mon. Wea. Rev.*, *106*, 223-232, 1978.

Gaynor, J. E., and C. F. Ropelewski, Analysis of the convectively modified GATE boundary layer using *in situ* and acoustic sounder data, *Mon. Wea. Rev.*, *107*, 985-993, 1979.

Goff, R. C., Vertical structure of thunderstorm outflows, *Mon. Wea. Rev.*, *104*, 1429-1440, 1976.

Gray, W. M., Cumulus convection and larger scale circulations: I. Broad scale and mesoscale considerations, *Mon. Wea. Rev.*, *101*, 839-855, 1973.

Harshvardhan, D. A. Randall, T. G. Corsetti, and D. A. Dazlich, Earth radiation budget and cloudiness simulations with a general circulation model, *J. Atmos. Sci.*, *46*, 1922-1942, 1989.

Heymsfield, G. M., Evolution of downdrafts and rotation in an Illinois thunderstorm, *Mon. Wea. Rev.*, *109*, 1969-1988, 1981.

Houze, R. A., Structure and dynamic of a tropical squall-line system, *Mon. Wea. Rev.*, 105, 1540-1567, 1977.

_______, and A. K. Betts, Convection in GATE, *Rev. Geophys. Space Phys.*, *19*, 541-576, 1981.

_______, and P. V. Hobbs, Organization and structure of precipitating cloud systems, *Advances in Geophysics*, *Vol. 24*, Academic Press, 225-315, 1982.

Johnson, R. H., The role of convective-scale precipitation downdrafts in cumulus and synoptic-scale interactions, *J. Atmos. Sci.*, *33*, 1890-1910, 1976.

_______, Large-scale effects of deep convection on the GATE tropical boundary layer, *J. Atmos. Sci.*, *38*, 2399-2413, 1981.

_______, and G. S. Young, Heat and moisture budgets of tropical mesoscale anvil clouds, *J. Atmos. Sci.*, *40*, 2138-2147, 1983.

Johnson, R. H. and M. E. Nicholls, A composite analysis of the boundary layer accompanying a tropical squall line, *Mon. Wea. Rev.*, *111*, 308-319, 1983.

Klemp, J. B., R. B. Wilhelmson, and P. Ray, Observed and numerically simulated structure of a mature super cell thunderstorm, *J. Atmos. Sci.*, 38, 1558-1580, 1981.

Knupp, K. R. and W. R. Cotton, An intense, quasi-steady thunderstorm over mountainous terrain. Part II: Doppler radar observations of the storm morphological structure, *J. Atmos. Sci.*, *39*, 343-358, 1982.

Krueger, S. K., Numerical simulation of tropical cumulus clouds and their interaction with the subcloud layer, *J. Atmos. Sci.*, *45*, 2221-2250, 1988:.

Leary, C. A., Temperature and humidity profiles in mesoscale unsaturated downdrafts, *J. Atmos. Sci.*, *37*, 1005-1012, 1980.

Leary, C. A., and R. A. Houze, The structure and evolution of convection in a tropical cloud cluster, *J. Atmos. Sci.,* 36, 437-457, 1979a.

----,and---, Melting and evaporation of hydrometeors in precipitation from the anvil clouds of deep tropical convection, *J. Atmos. Sci.*, *36*, 669-679, 1979b.

Ludlam, F. H., Severe local storm: A review. *Meteor. Monogr.*, *5*, 1-30, 1963.

Miller, M. J., and A. K. Betts, Traveling convective storms over Venezuela, *Mon. Wea. Rev.*, *105*, 833-848, 1977.

Molinari, J., and T. Corsetti, Incorporation of cloud-scale and meso-scale downdrafts into a cumulus parameterization: Results of one- and three-dimensional integrations, *Mon. Wea. Rev.*, *113*, 485-501, 1985.

Newton, C. W., Circulations in large sheared cumulonimbus, *Tellus*, *18*, 699-713, 1966.

Nicholls, M. E. and R. H. Johnson, A model of a tropical squall line boundary layer wake, *J. Atmos. Sci.*, *41*, 2774-2792, 1984.

Nitta, T., and S. Esbensen, Heat and moisture budgets using BOMEX data, *Mon. Wea. Rev.*, *102*, 17-28, 1975.

Nitta, T., Response of cumulus updraft and downdraft to GATE A/B-scale motion systems, *J. Atmos. Sci.*, *34*, 1163-1186, 1977.

Ogura, Y., and H.R. Cho, Diagnostic determination of cumulus cloud populations from large-scale variables, *J. Atmos. Sci.*, *30*, 1276-1286, 1973.

Ogura, Y., and M. T. Liou, The structure of a mid-latitude squall line: A case study, *J. Atmos. Sci.*, *37*, 553-567, 1980.

Randall, D. A. and D. M. Pan, Implementation of the Arakawa-Schubert cumulus parameterization with a prognostic closure, in *Cumulus Parameterization*, a Meteorological Monograph published by the American Meteorological Society, 137-144, 1993.

Randall, D. A., Harshvardhan, D. A. Dazlich, and T. G. Corsetti, Interactions Among Radiation, Convection, and Large-Scale Dynamics in a General Circulation Model, *J. Atmos. Sci.*, *46*, 1943-1970, 1989.

Randall, D. A., Harshvardhan, and D. A. Dazlich, Diurnal variability of the hydrologic cycle in a general circulation model, *J. Atmos. Sci.*, *48*, 40-62, 1991.

Rossow, W. B., and R. A. Schiffer, The International Satellite Cloud Climatology Project (ISCCP): The first project of the World Climate Research Program, *Bull. Amer. Meteor. Soc.*, *64*, 779-784, 1983.

Sellers, P. J, D. A. Randall, J. A. Collatz, J. A. Berry, C. B. Field, D. A. Dazlich, and G. D. Collelo, A revised land-surface parameterization (SiB2) for GCMs. Part I: Model formulation, Submitted to *J. Clim.*, 1994.

Sud, Y. C. and G. K. Walker, A rain evaporation and downdraft parameterization to complement a cumulus updraft scheme and its evaluation using GATE data, *Mon. Wea. Rev.*, *121*, 3019-3039, 1993.

Suarez, M. J., A. Arakawa, and D. A. Randall, Parameterization of the planetary boundary layer in the UCLA general circulation model: Formulation and results, *Mon. Wea. Rev.*, *111*, 2224-2243, 1983.

Takeda, T., Numerical simulation of a precipitating convective cloud: The formation of a "long-lasting" cloud, *J. Atmos. Sci.*, *28*, 350-376, 1971.

Tiedtke M., A comprehensive mass flux scheme for cumulus parameterization in large-scale models, *Mon. Wea. Rev.*, *117*, 1779-1800, 1989.

Wade, C. G. and G. B. Foote, Low-level airflow and mesoscale influences, in *Hailstorms of the Central High Plains, Vol. 2,* edited by C. Knight and P. Squires, Colo. Assoc. Univ. Press, 115-130, 1982.

Wu, X., Effects of mesoscale convective organization and vertical wind shear on the cumulus-environment interaction, Ph.D. dissertation, 221 pp., Department of Atmospheric Sciences, University of California, Los Angeles, CA, 1992.

Yanai, M., S. Esbensen and J.-H. Chu, Determination of bulk properties of tropical clusters from large scale heat and moisture budgets, *J. Atmos. Sci.*, *30*, 611-637, 1973.

_______, J. H. Chu, T. E. Stark and T. Nitta, Response of deep and shallow tropical maritime cumuli to large-scale processes. *J. Atmos. Sci.*, *33*, 976-991, 1976.

Young, G. S. and D. V. Ledvina, Influence of precipitating convection on the surface energy budget observed during a tropical ocean atmosphere pilot cruise in the Tropical Western Pacific Ocean, *J. Atmos.* Sci., *97*, 9595-9603, 1992.

Zipser, E. J., The role of organized unsaturated convective downdrafts in the structure and rapid decay of an equatorial disturbance, *J. Appl. Meteor.*, *8*, 799-814, 1969.

_______, Mesoscale and convective-scale downdrafts as distinct components of squall-line structure, *Mon. Wea. Rev.*, *105*, 1568-1589, 1977.

Figure Captions

Figure 1: Global maps of the monthly mean cumulus incidence with CUPDW and the difference between CUPDW and CONTROL. The contour interval is 0.1 (0.05 for the difference field). Heavy shading corresponds to values greater than 0.5 (greater than 0 for the difference field).

Figure 2: Latitude-pressure cross sections of the monthly mean cumulus detrainment mass flux simulated by CUPDW and the difference. Units are hr^{-1}, and the contour interval is 0.01 (0.001 for the difference field). Heavy shading corresponds to values greater than 0.06 (greater than 0 for the difference plot).

Figure 3: Latitude-pressure cross sections of the monthly mean cumulus heating rates simulated by CUPDW and the difference between CUPDW and CONTROL. Units are K day^{-1}, and the contour interval is 0.2 K day^{-1} (0.1 for the difference field). Heavy shading corresponds to values greater than 1.1 K day^{-1} (less than 0 for the difference plot).

Figure 4: Latitude-pressure cross sections of the monthly mean cumulus moistening rates simulated by CUPDW and the difference between CUPDW and CONTROL. Units are g $kg^{-1}day^{-1}$, and the contour interval is 0.1 (0.02 for the difference field). Heavy shading corresponds to values greater than 0 (greater than 0 for the difference plot). Light shading corresponds to values less than - 0.4.

Figure 5: Global maps of cumulus precipitation simulated by CUPDW and the difference between CUPDW and CONTROL. Units are mm day^{-1}, and the contour interval is 2 (0.5 for the difference plot). Heavy shading corresponds to values greater than 8 (greater than 0 for the difference plot).

Figure 6: Global scatter diagram: change in PBL depth (a) and PBL specific humidity (b) between CUPDW and CONTROL vs. cumulus precipitation in CUPDW.

Figure 7: Global maps of relative humidity at the PBL top as simulated by CUPDW and the difference between CUPDW and CONTROL. The contour interval is 0.2 (0.05 for the difference plot). Heavy shading corresponds to values greater than 1. (greater than 0 for the difference plot).

Figure 8: Global maps of PBL cloud depth simulated by CUPDW and the difference between CUPDW and CONTROL. The contour interval is 10 (3 for the difference plot). Heavy shading corresponds to values greater than 20 (greater than 0 for the difference plot).

Figure 9: Global maps of PBL wind speed as simulated by CUPDW and the difference between CUPDW and CONTROL. The contour interval is 40 (10 for the difference plot). Heavy shading corresponds to values greater than 180 (greater than 0 for the difference plot).

Figure 10: Latitude-pressure cross sections of the monthly mean temperature simulated with CUPDW and the difference between CUPDW and CONTROL. Units are K, and the contour interval is 5 (0.2 for the difference plot). Heavy shading corresponds to values greater than 290 (greater than 0 in the difference fields).

Figure 11: Latitude-pressure cross sections of specific humidity simulated with CUPDW, and the difference between CUPDW and CONTROL. Units are g kg^{-1}, and the contour interval is 1 (0.05 for the difference plot). Heavy shading corresponds to values greater than 10 (greater than 0 for the difference plot).

Figure 12: Latitude-pressure cross sections of zonal wind simulated with CUPDW and the difference between CUPDW and CONTROL. Units are m s^{-1}, and the contour interval is 5 (0.5 for the difference plot). Heavy shading corresponds to values greater than 30 (greater than 0 for the difference plot). Light shading corresponds

values less than 0.

Figure 13: Global maps of the monthly mean total precipitation simulated with CONTROL and climate data from Legates and Willmott (1990), and the difference between these two plots. Units are mm day^{-1}, and the contour interval is 2 (1 for the difference plot). Heavy shading corresponds to values greater than 8 (0 for the difference plot).

Figure 14: Global maps of the monthly mean total precipitation simulated with CUPDW and the difference between these CUPDW and CONTROL. Units are mm day $^{-1}$, and the contour is 22 (1 for the difference plot). Heavy shading corresponds to values greater than 8 (0 for the difference plot).

Figure 15: Global maps of the monthly mean net longwave surface flux simulated with CUPDW and the difference between CUPDW and CONTROL. Units are W m^{-2}, and the contour interval is 15 (10 for the difference plot). Heavy shading corresponds to values greater than 60 (0 for the difference plot).

Figure 16: Global maps of the monthly mean net shortwave surface flux simulated with CUPDW and the difference between CUPDW and CONTROL. Units are W m^{-2}, and the contour interval is 40 (10 for the difference plot). Heavy shading corresponds to values greater than 240 (0 for the difference plot).

Figure 17: Global maps of the monthly mean surface sensible heat flux simulated with CUPDW and the difference between CUPDW and CONTROL. Units are W m^{-2}, and the contour interval is 20 (10 for the difference plot). Heavy shading corresponds to values greater than 0 (0 for the difference plot).

Figure 18: Global maps of the monthly mean latent heat flux simulated with CUPDW and the difference between CUPDW and CONTROL. Units are W m^{-2}, and the contour interval is 40 (10 for the difference plot). Heavy shading corresponds to values greater than 120 (0 for the difference plot).

Figure 19: Zonally averaged distributions of the difference of the monthly averaged net downward surface flux, surface longwave radiative flux, surface shortwave radiative flux, surface latent heat flux and surface sensible heat flux simulated with CONTROL and CUPDW. Units are W m^{-2}.

Figure 20: Latitudes-pressure cross sections of the monthly mean cumulus heating rates (a) and moistening rates (b) simulated by EXP2. Units are K day^{-1} in (a) and g kg^{-1} day^{-1}. Heavy shading corresponds to values greater than 1.1 in (a) and 0. in (b). Light shading in (b) corresponds to values less than -0.4.

Figure 21: Difference plots of zonal mean zonal wind between CUPDW and ECMWF (a), EXP3 and CUPDW (b). Units are m s^{-1}. Heavy shading in (b) corresponds to value greater than 0. Light shading in (a) corresponds to values less than 0.

Figure 22: Global scatter diagram: change in PBL wind speed (a) and latent heat flux (b) between EXP3 and CUPDW vs. cumulus precipitation in CUPDW.

Figure 23: Model for updraft and downdraft of cloud type λ, based on Johnson (1976).

Figure 24: The vertical structure of the *i*th cloud type, based on Lord et al. (1982). Entrainment E takes place at all integer levels including the cloud-top level, while detrainment D takes place at the cloud-top level only. The sub-ensemble vertical mass flux M is stored at the half-integer and is normalized at cloud base (level $KF+1/2$).

Cumulus Incidence

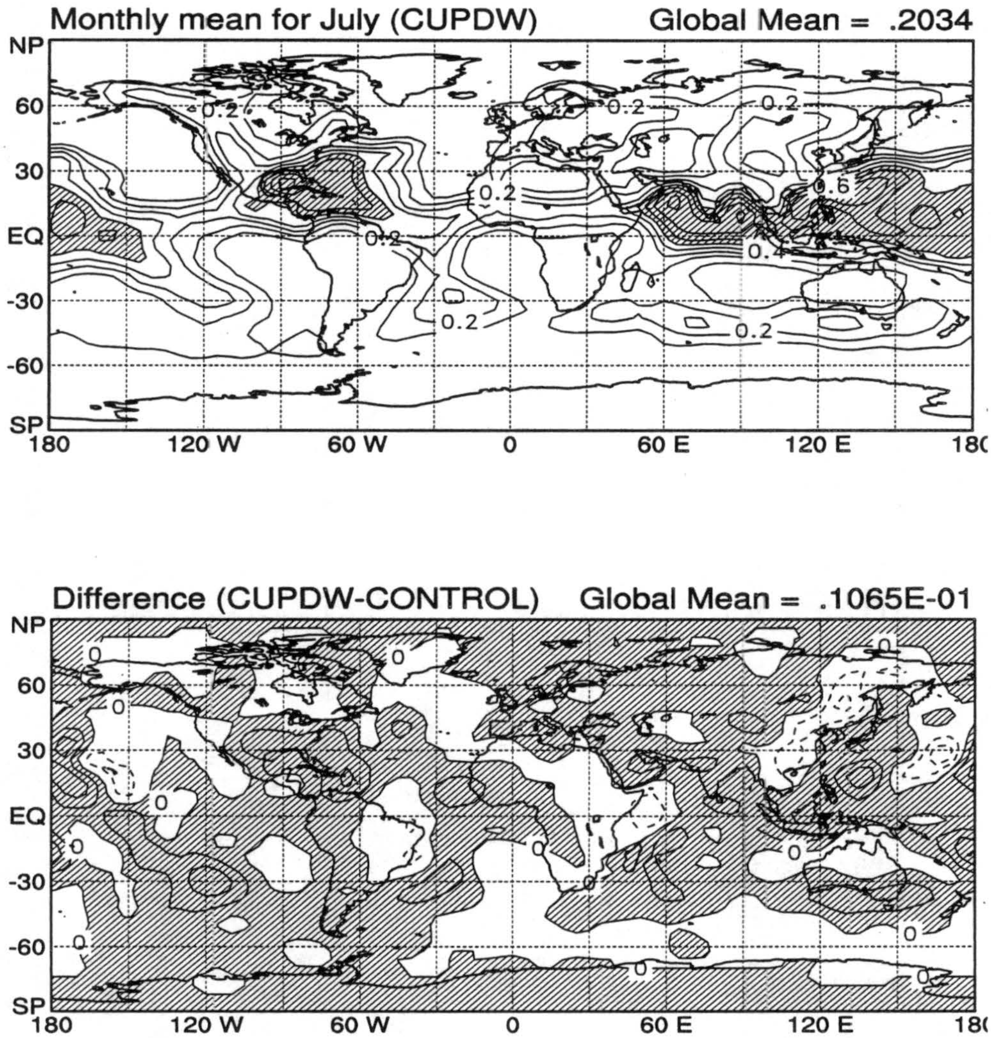

Figure 1: Global maps of the monthly mean cumulus incidence with CUPDW and the difference between CUPDW and CONTROL. The contour interval is 0.1 (0.05 for the difference field). Heavy shading corresponds to values greater than 0.5 (greater than 0 for the difference field).

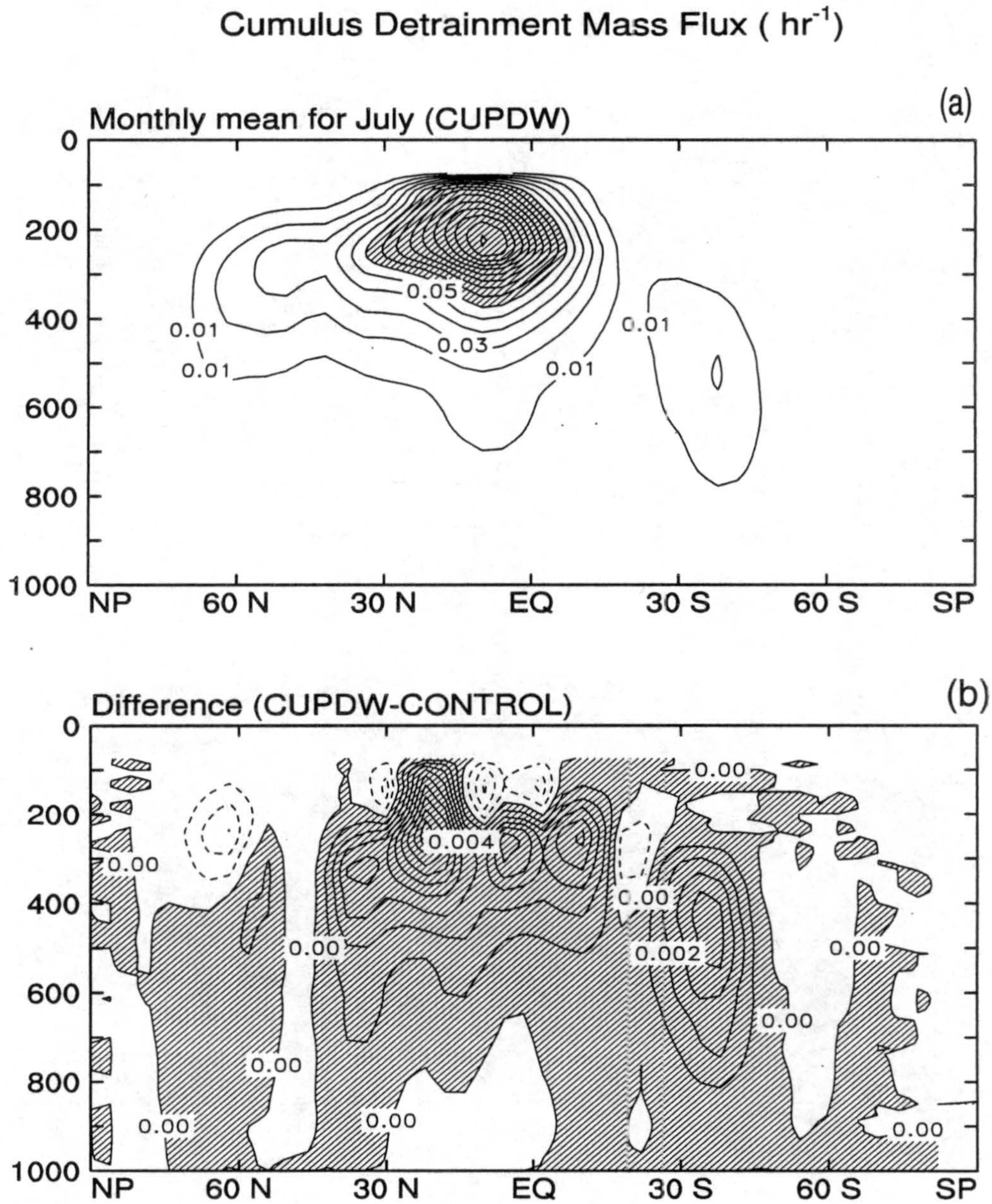

Figure 2: Latitude-pressure cross sections of the monthly mean cumulus detrainment mass flux simulated by CUPDW and the difference. Units are hr^{-1}, and the contour interval is 0.01 (0.001 for the difference field). Heavy shading corresponds to values greater than 0.06 (greater than 0 for the difference plot).

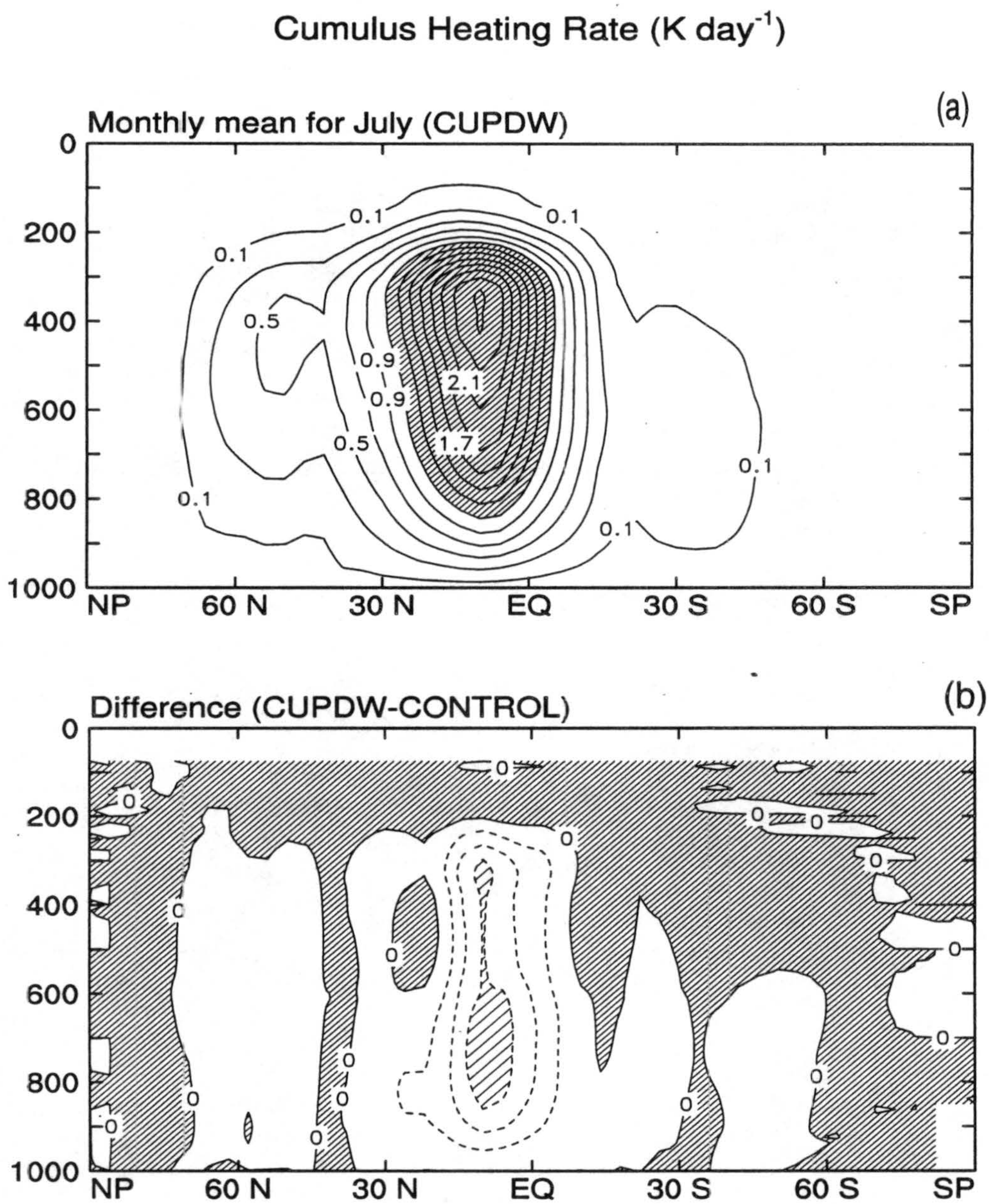

Figure 3: Latitude-pressure cross sections of the monthly mean cumulus heating rates simulated by CUPDW and the difference between CUPDW and CONTROL. Units are K day^{-1}, and the contour interval is 0.2 K day^{-1} (0.1 for the difference field). Heavy shading corresponds to values greater than 1.1 K day^{-1} (less than 0 for the difference plot).

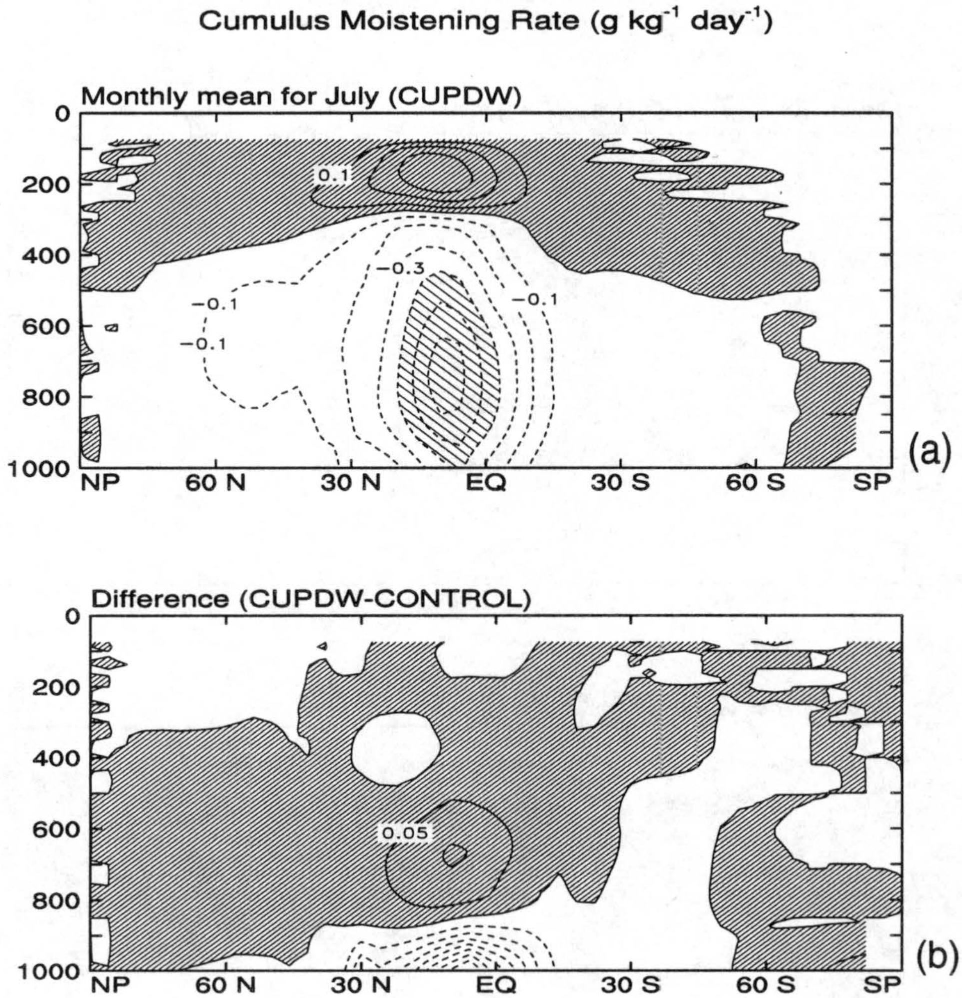

Figure 4: Latitude-pressure cross sections of the monthly mean cumulus moistening rates simulated by CUPDW and the difference between CUPDW and CONTROL. Units are g $kg^{-1}day^{-1}$, and the contour interval is 0.1 (0.02 for the difference field). Heavy shading corresponds to values greater than 0 (greater than 0 for the difference plot). Light shading corresponds to values less than - 0.4.

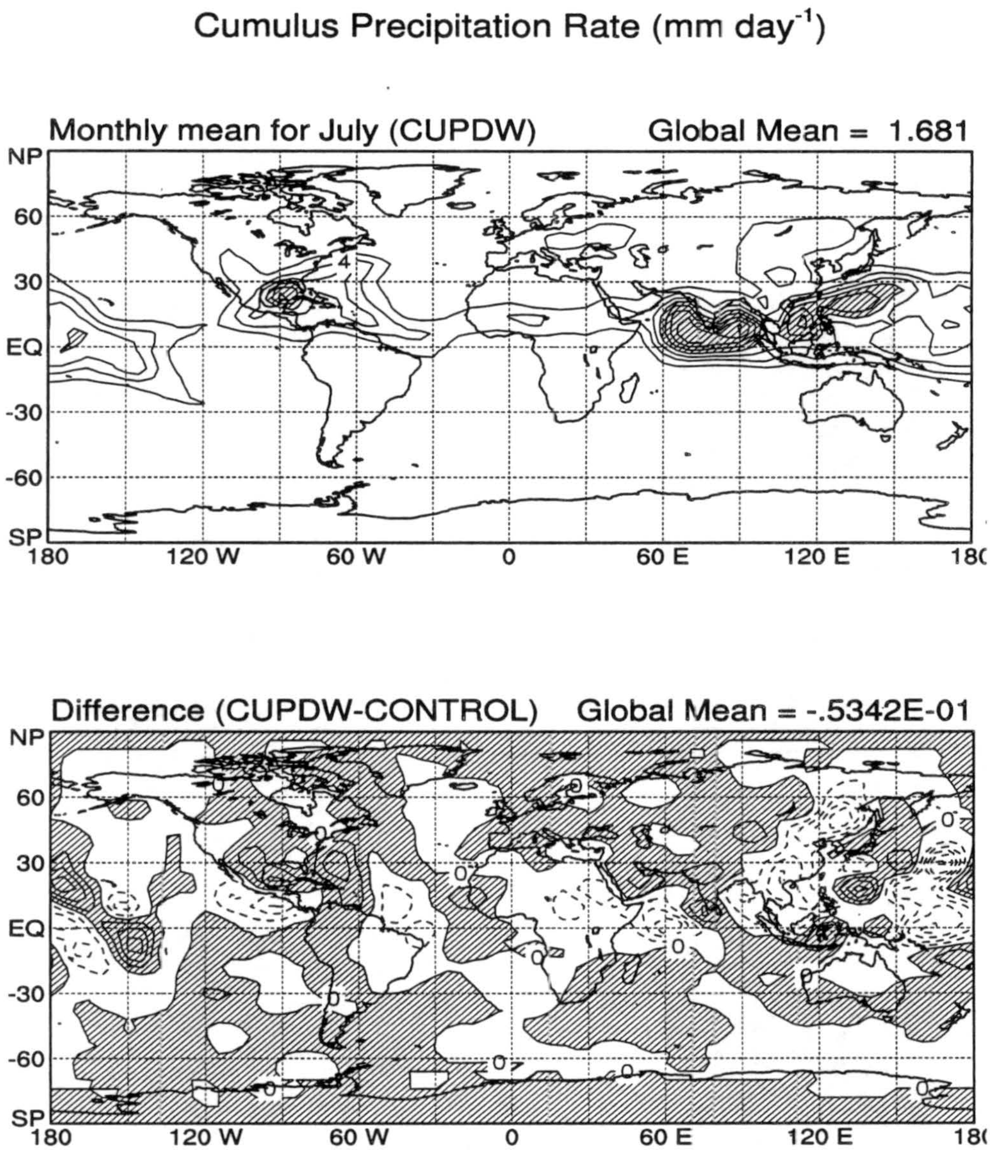

Figure 5: Global maps of cumulus precipitation simulated by CUPDW and the difference between CUPDW and CONTROL. Units are mm day^{-1}, and the contour interval is 2 (0.5 for the difference plot). Heavy shading corresponds to values greater than 8 (greater than 0 for the difference plot).

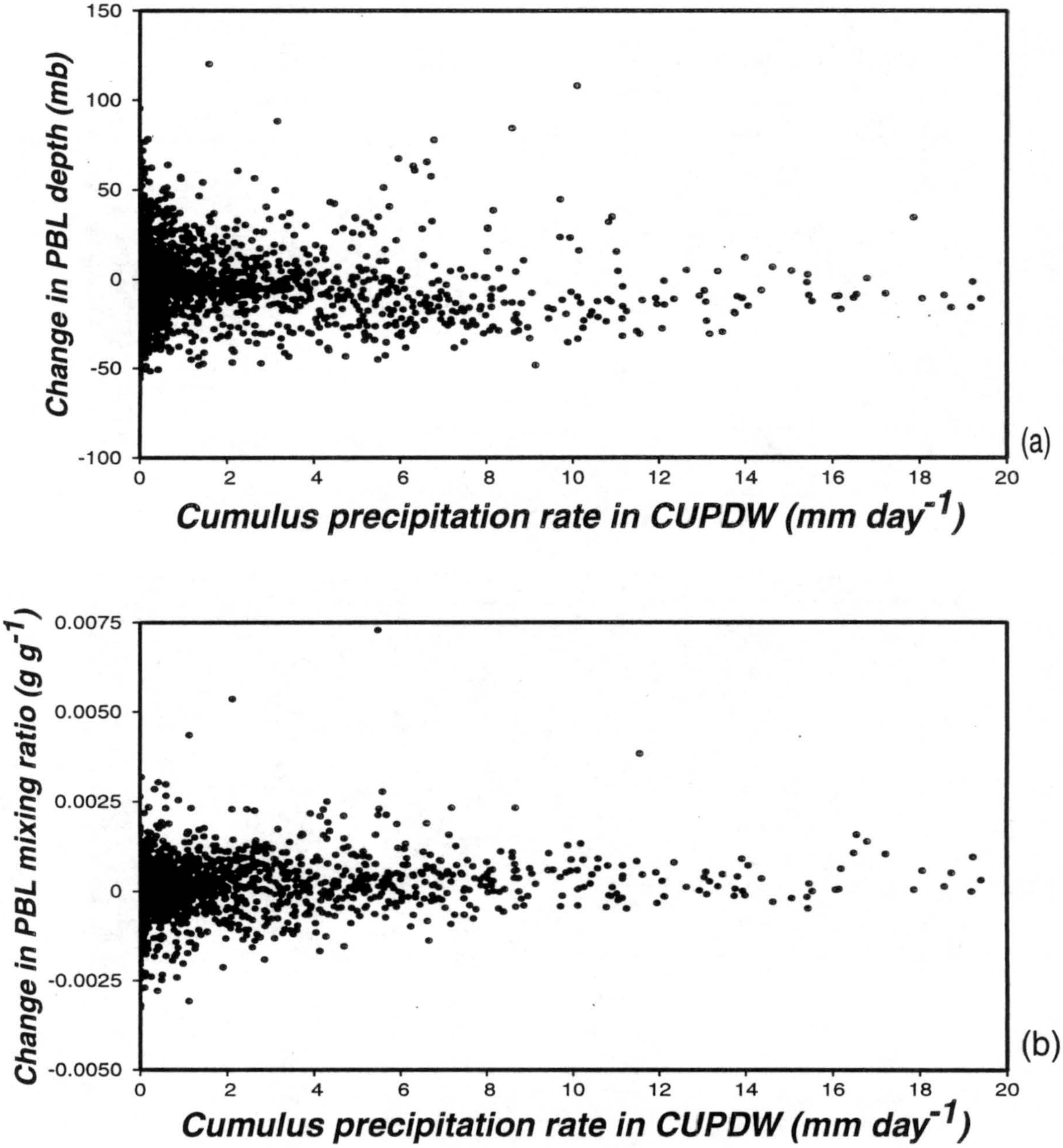

Figure 6: Global scatter diagram: change in PBL depth (a) and PBL specific humidity (b) between CUPDW and CONTROL vs. cumulus precipitation in CUPDW.

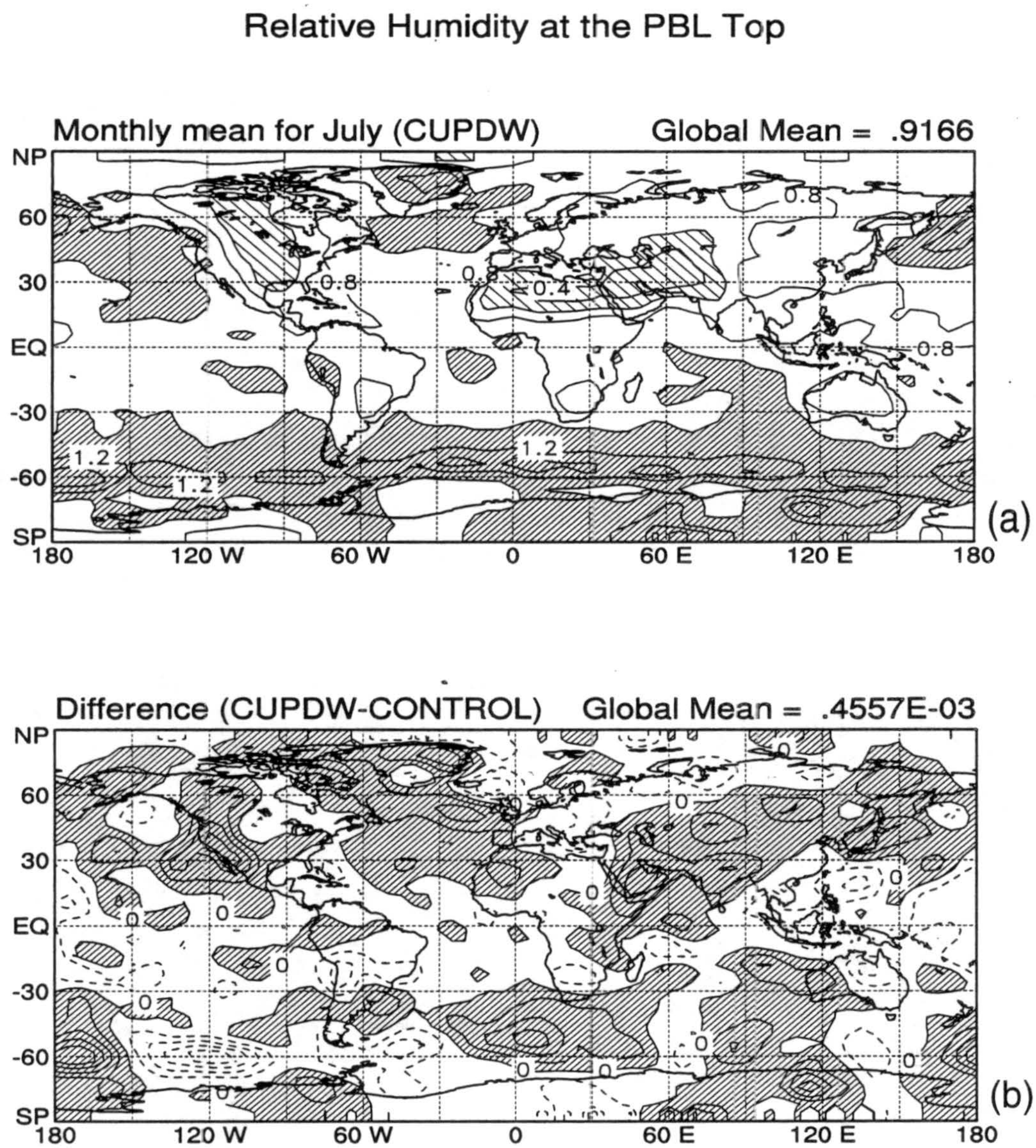

Figure 7: Global maps of relative humidity at the PBL top as simulated by CUPDW and the difference between CUPDW and CONTROL. The contour interval is 0.2 (0.05 for the difference plot). Heavy shading corresponds to values greater than 1. (greater than 0 for the difference plot).

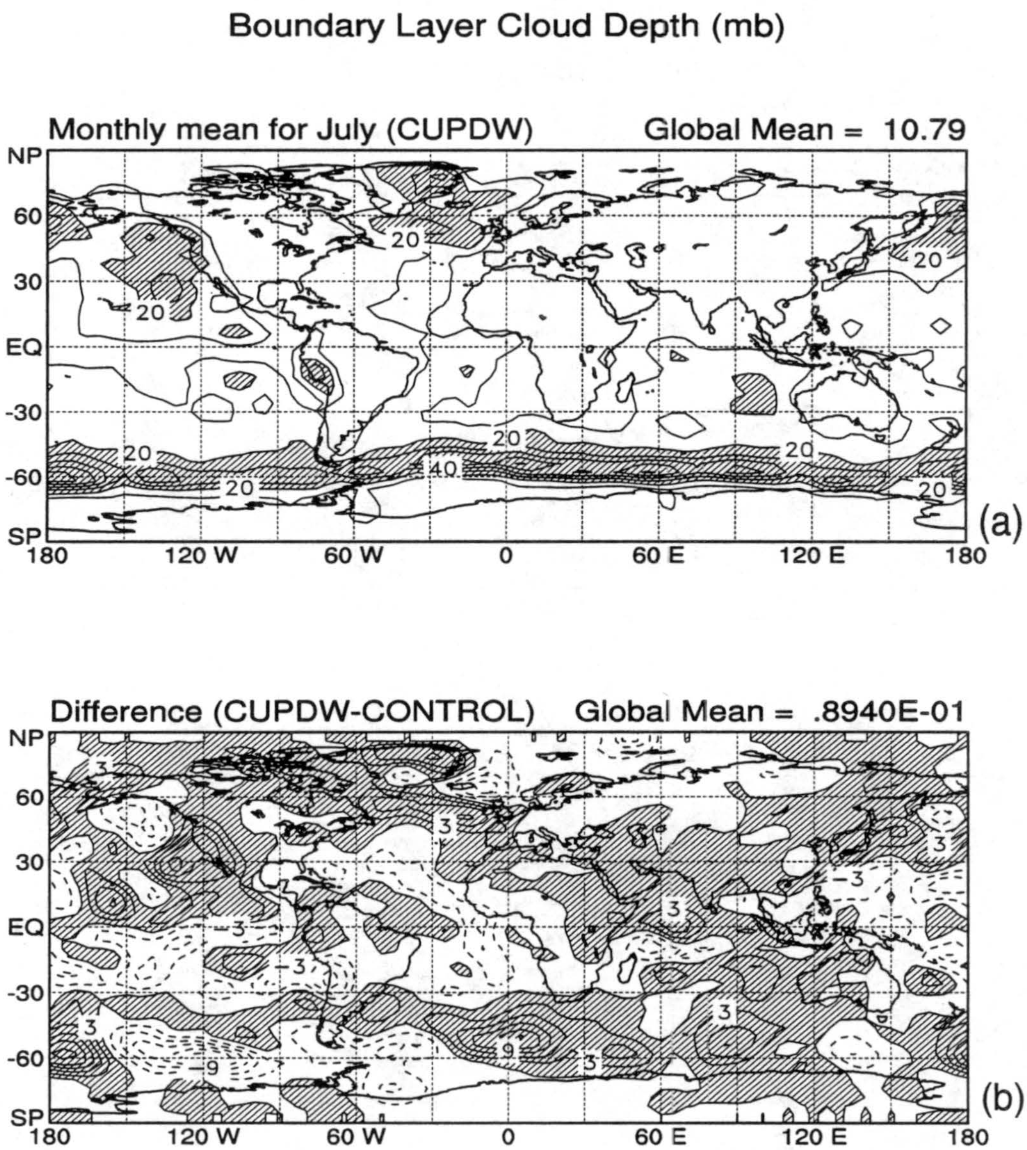

Figure 8: Global maps of PBL cloud depth simulated by CUPDW and the difference between CUPDW and CONTROL. The contour interval is 10 (3 for the difference plot). Heavy shading corresponds to values greater than 20 (greater than 0 for the difference plot).

PBL Wind Speed (m s^{-1})

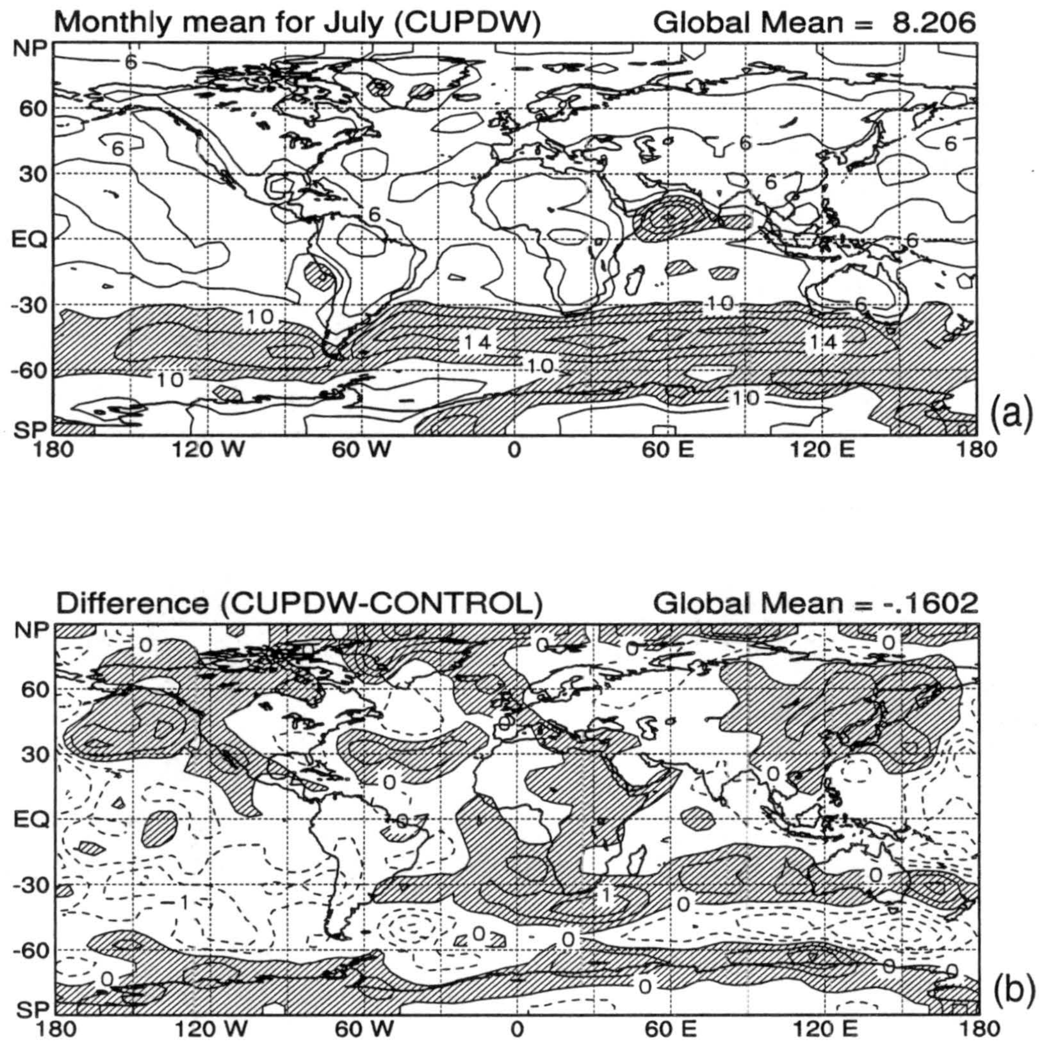

Figure 9: Global maps of PBL wind speed as simulated by CUPDW and the difference between CUPDW and CONTROL. The contour interval is 40 (10 for the difference plot). Heavy shading corresponds to values greater than 180 (greater than 0 for the difference plot).

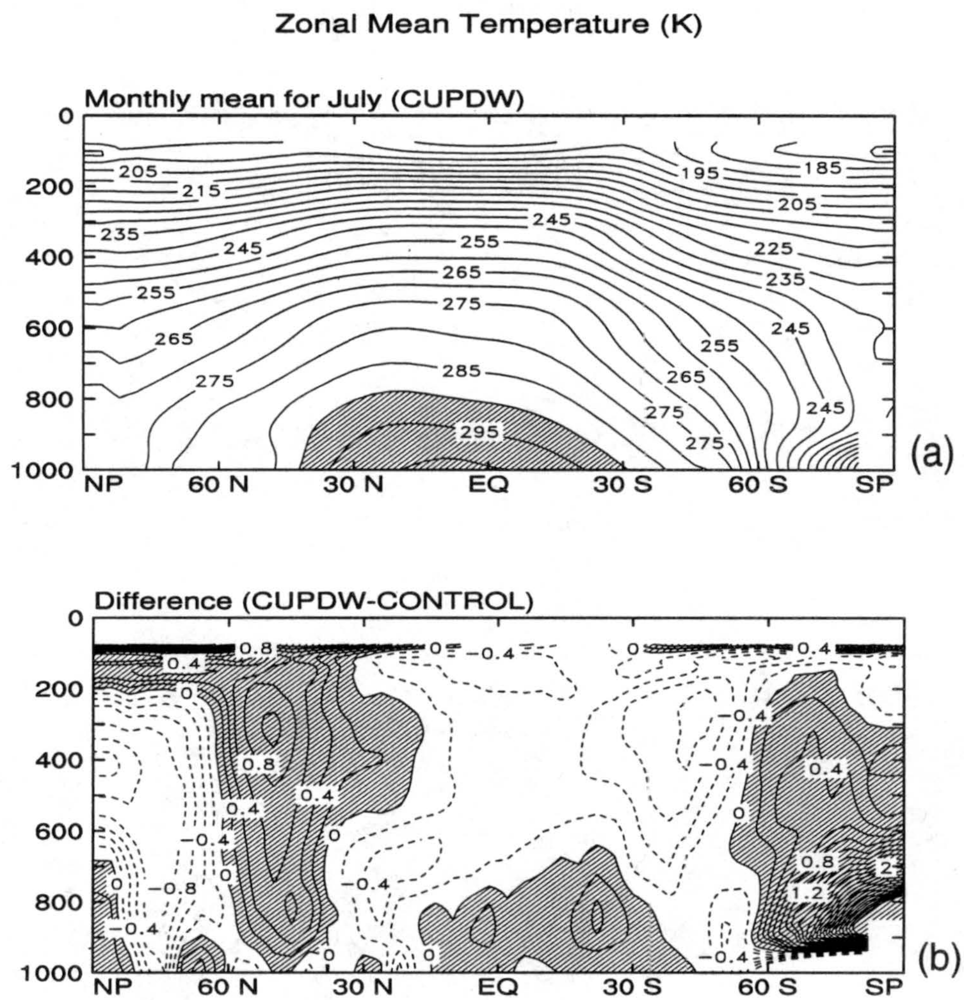

Figure 10: Latitude-pressure cross sections of the monthly mean temperature simulated with CUPDW and the difference between CUPDW and CONTROL. Units are K, and the contour interval is 5 (0.2 for the difference plot). Heavy shading corresponds to values greater than 290 (greater than 0 in the difference fields).

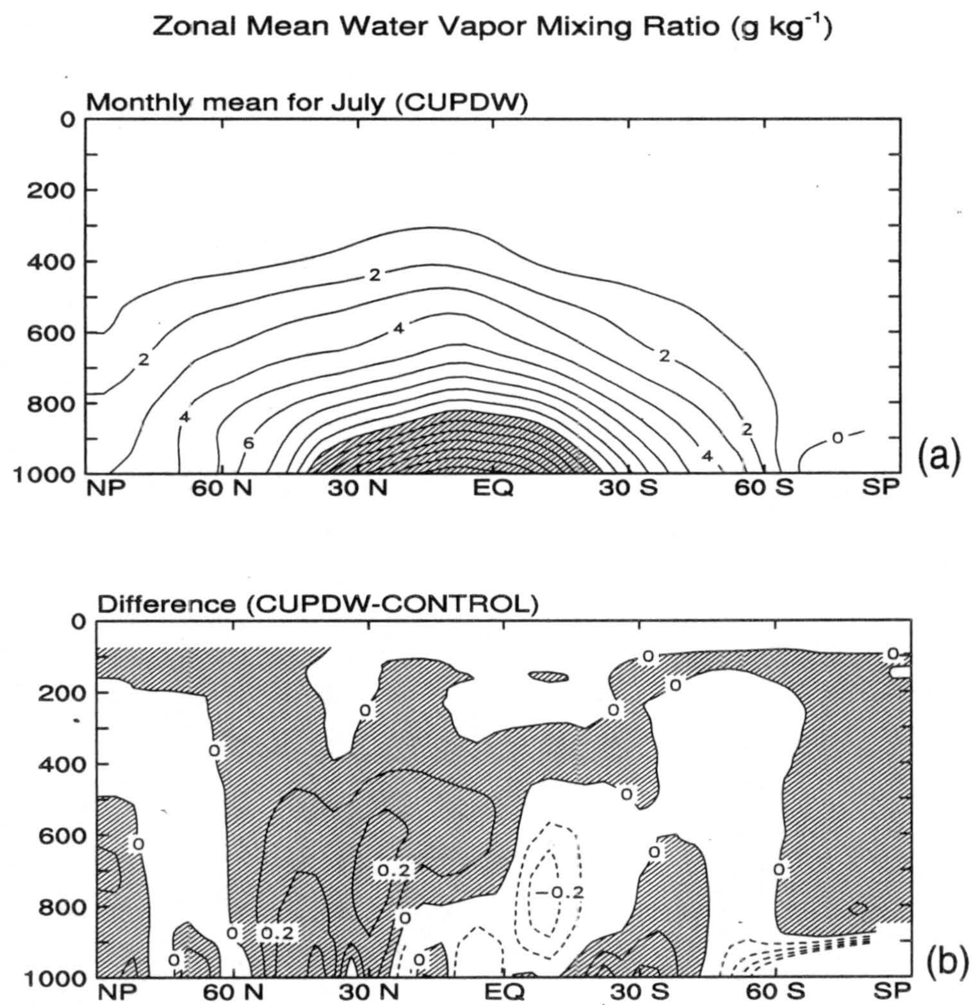

Figure 11: Latitude-pressure cross sections of specific humidity simulated with CUPDW, and the difference between CUPDW and CONTROL. Units are g kg^{-1}, and the contour interval is 1 (0.05 for the difference plot). Heavy shading corresponds to values greater than 10 (greater than 0 for the difference plot).

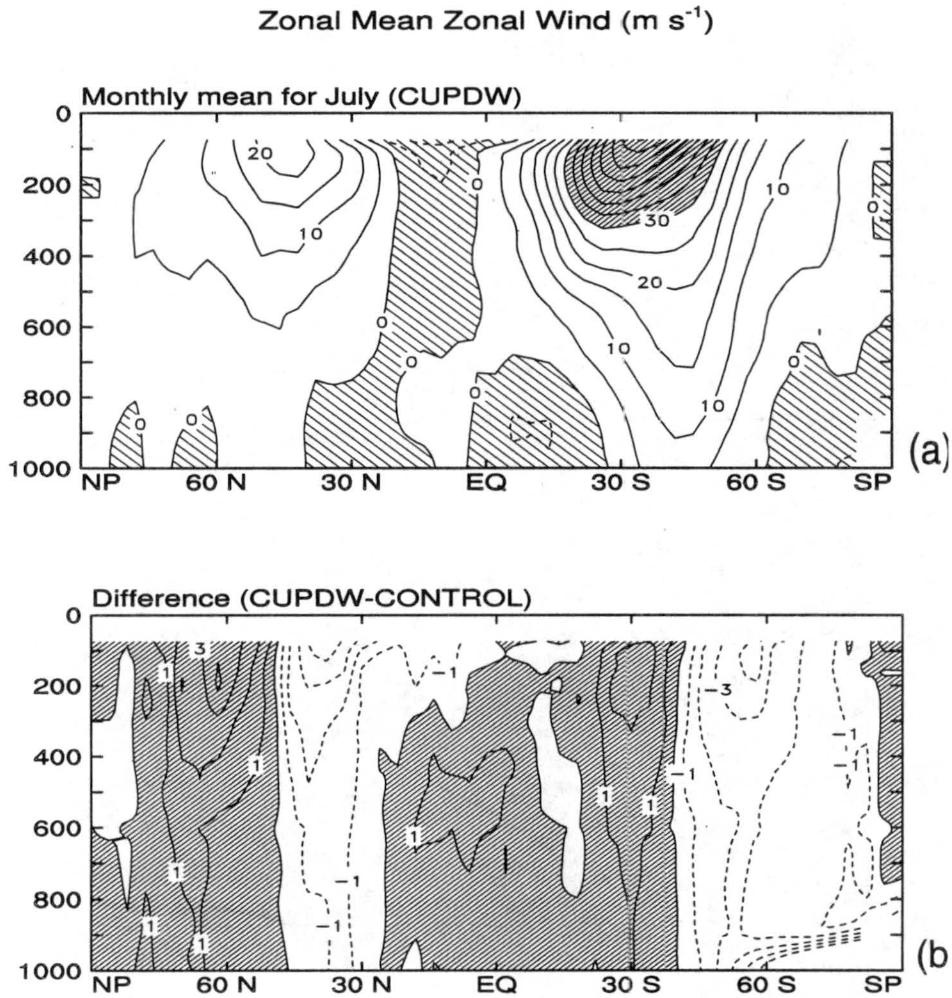

Figure 12: Latitude-pressure cross sections of zonal wind simulated with CUPDW and the difference between CUPDW and CONTROL. Units are m s^{-1}, and the contour interval is 5 (0.5 for the difference plot). Heavy shading corresponds to values greater than 30 (greater than 0 for the difference plot). Light shading corresponds values less than 0.

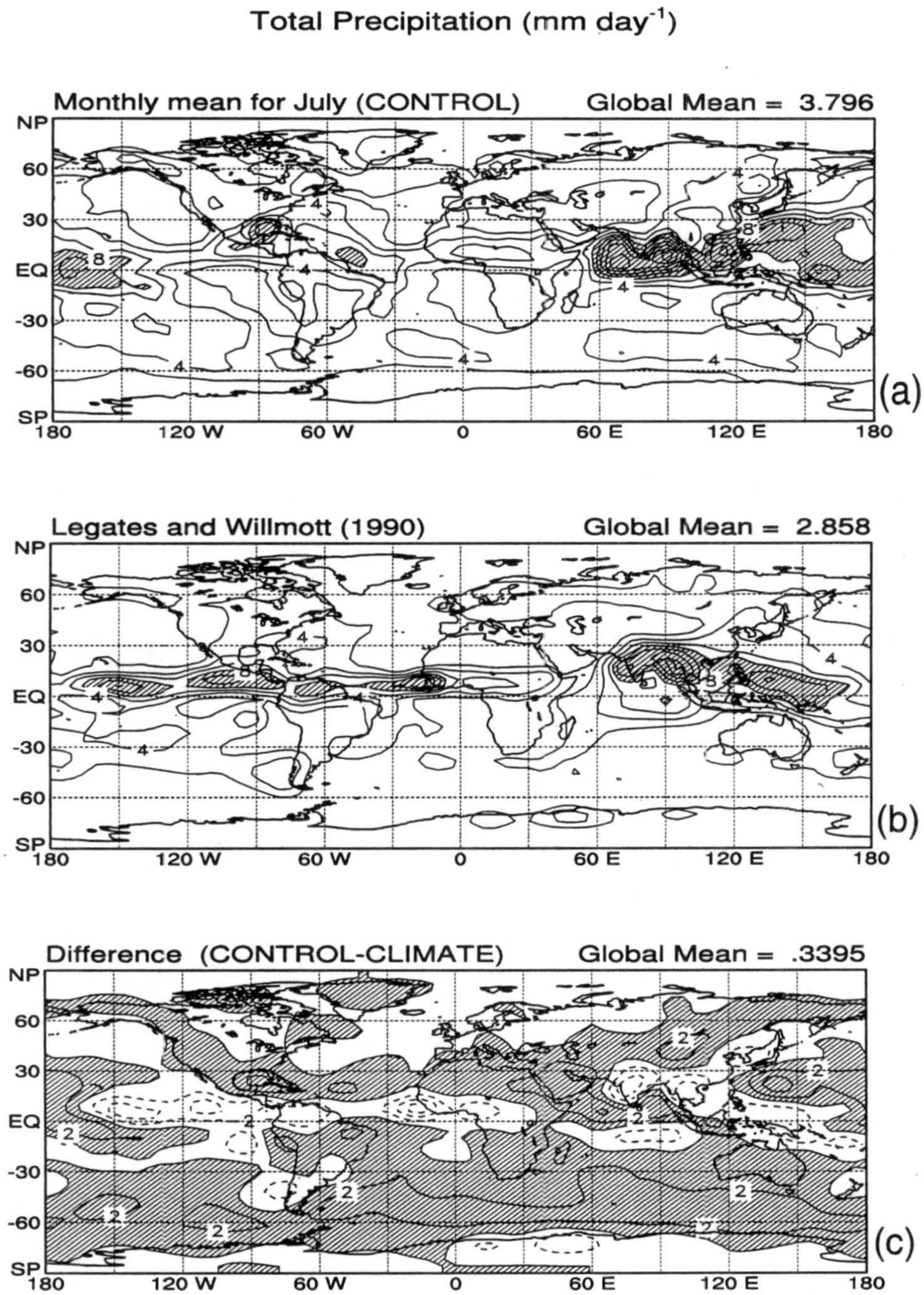

Figure 13: Global maps of the monthly mean total precipitation simulated with CONTROL and climate data from Legates and Willmott (1990), and the difference between these two plots. Units are mm day^{-1}, and the contour interval is 2 (1 for the difference plot). Heavy shading corresponds to values greater than 8 (0 for the difference plot).

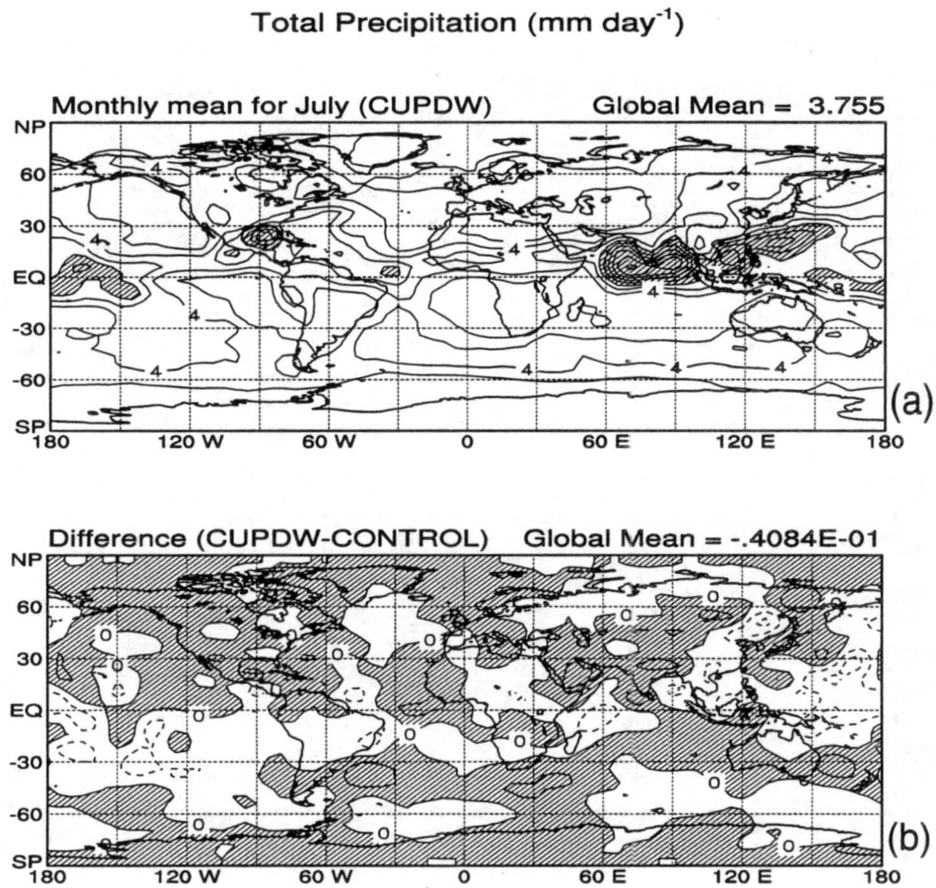

Figure 14: Global maps of the monthly mean total precipitation simulated with CUPDW and the difference between these CUPDW and CONTROL. Units are mm day $^{-1}$, and the contour is 22 (1 for the difference plot). Heavy shading corresponds to values greater than 8 (0 for the difference plot).

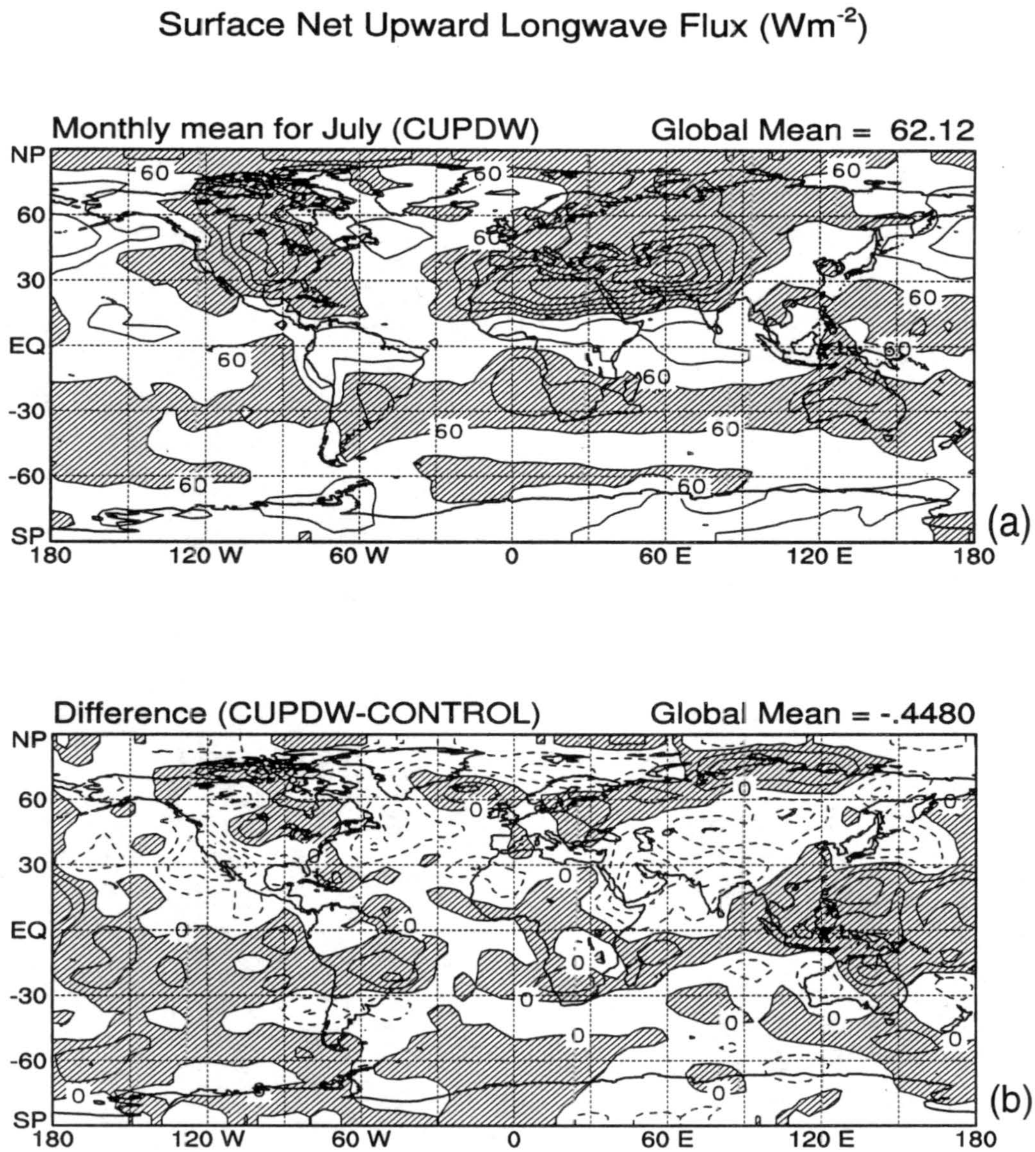

Figure 15: Global maps of the monthly mean net longwave surface flux simulated with CUPDW and the difference between CUPDW and CONTROL. Units are W m^{-2}, and the contour interval is 15 (10 for the difference plot). Heavy shading corresponds to values greater than 60 (0 for the difference plot).

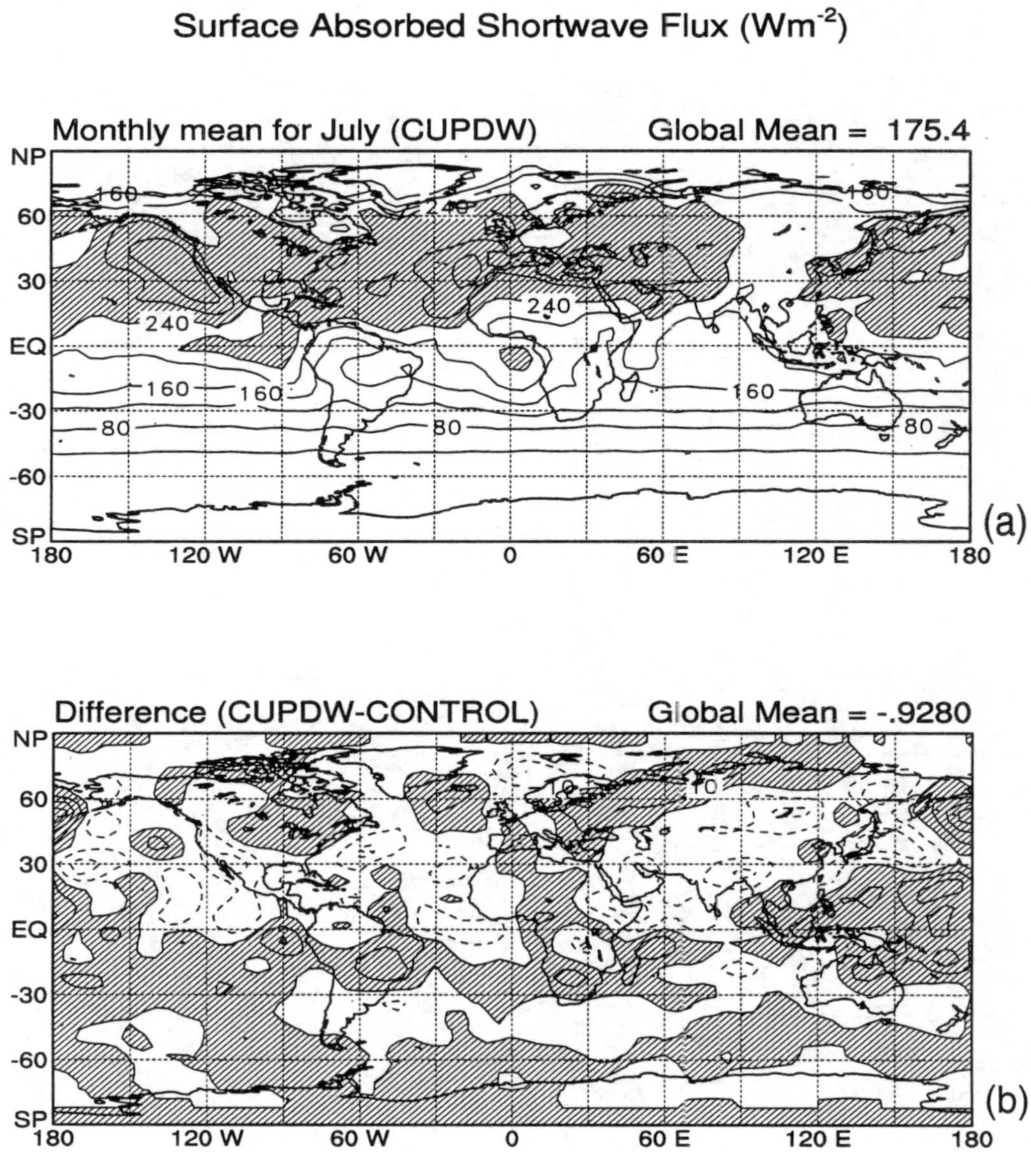

Figure 16: Global maps of the monthly mean net shortwave surface flux simulated with CUPDW and the difference between CUPDW and CONTROL. Units are W m^{-2}, and the contour interval is 40 (10 for the difference plot). Heavy shading corresponds to values greater than 240 (0 for the difference plot).

Surface Sensible Heat Flux (Wm^{-2})

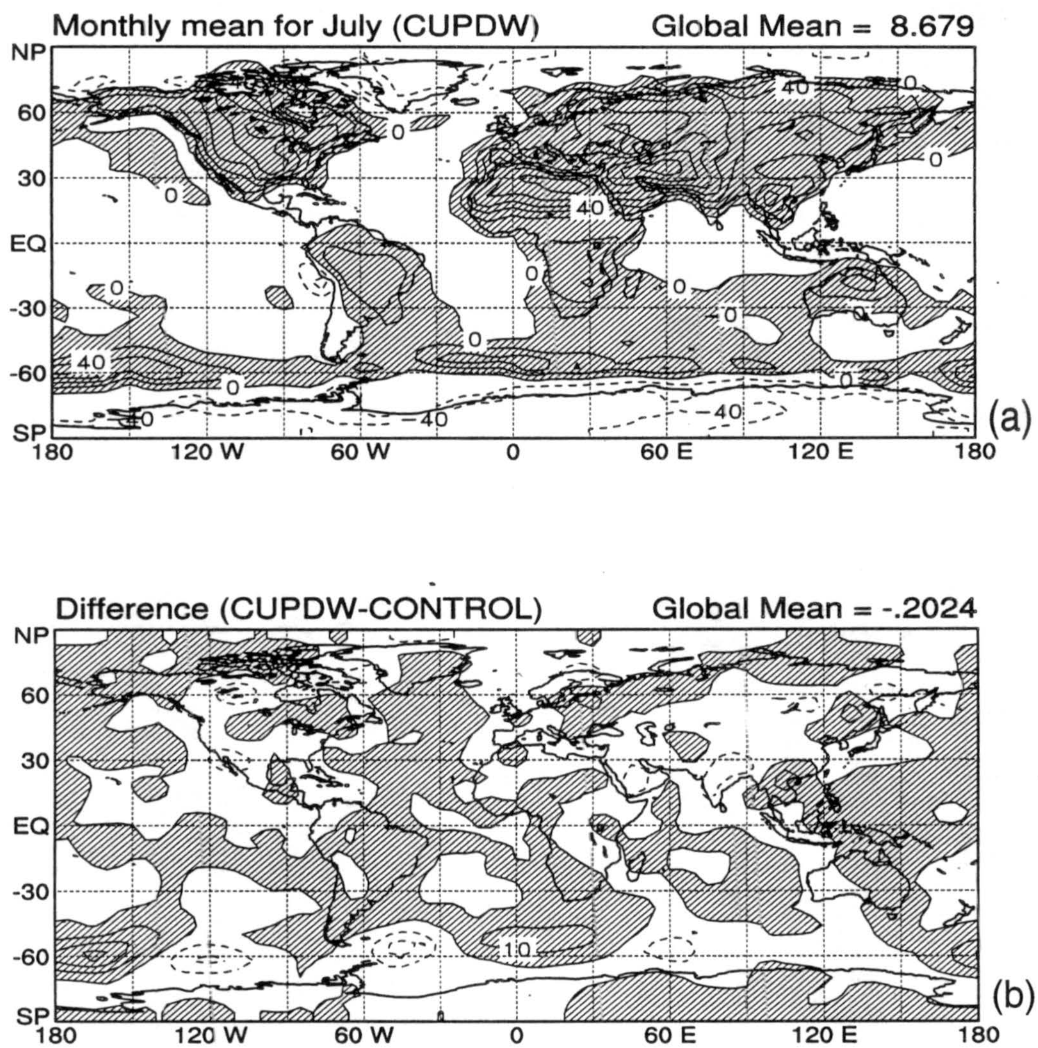

Figure 17: Global maps of the monthly mean surface sensible heat flux simulated with CUPDW and the difference between CUPDW and CONTROL. Units are W m^{-2}, and the contour interval is 20 (10 for the difference plot). Heavy shading corresponds to values greater than 0 (0 for the difference plot).

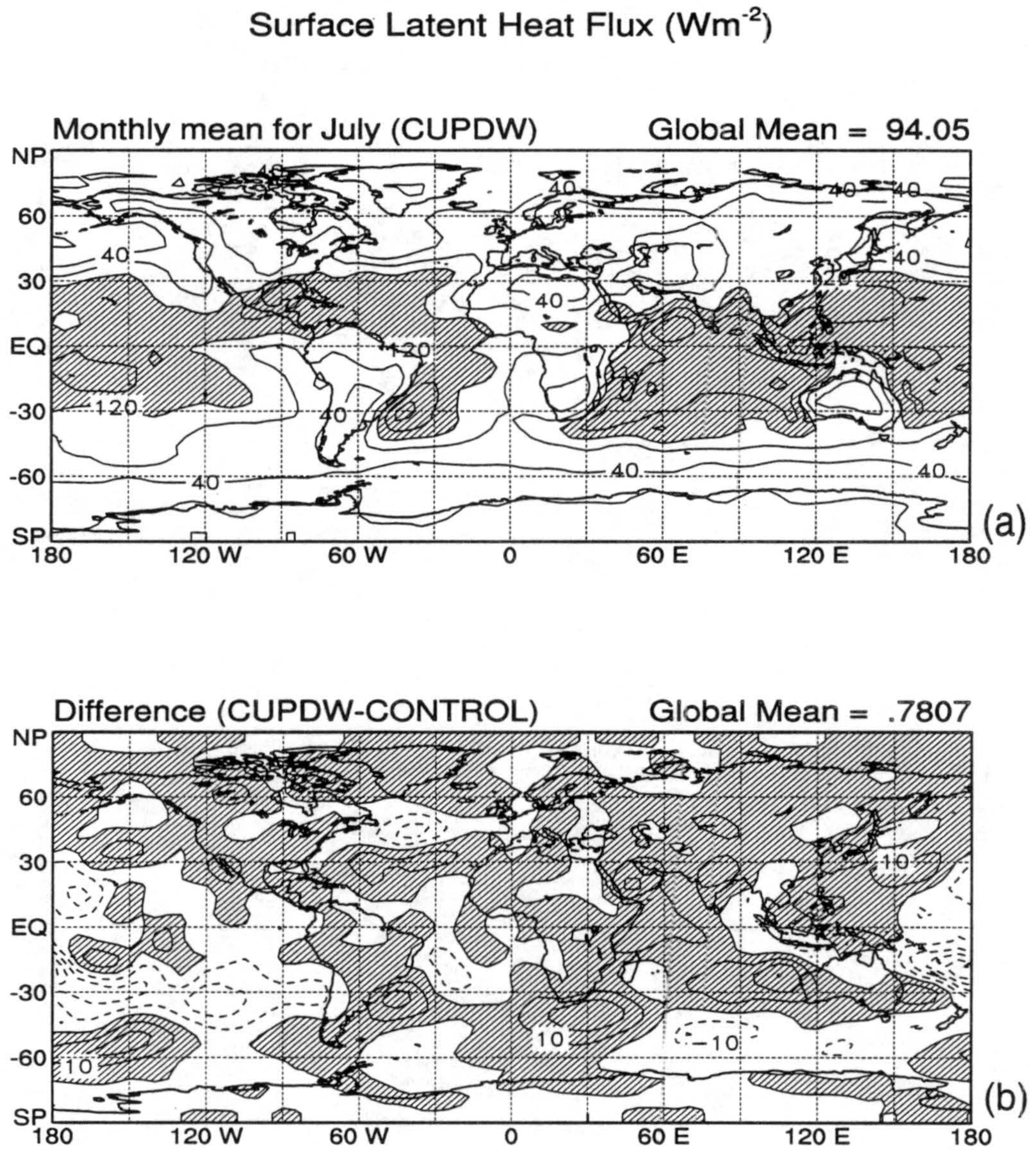

Figure 18: Global maps of the monthly mean latent heat flux simulated with CUPDW and the difference between CUPDW and CONTROL. Units are W m^{-2}, and the contour interval is 40 (10 for the difference plot). Heavy shading corresponds to values greater than 120 (0 for the difference plot).

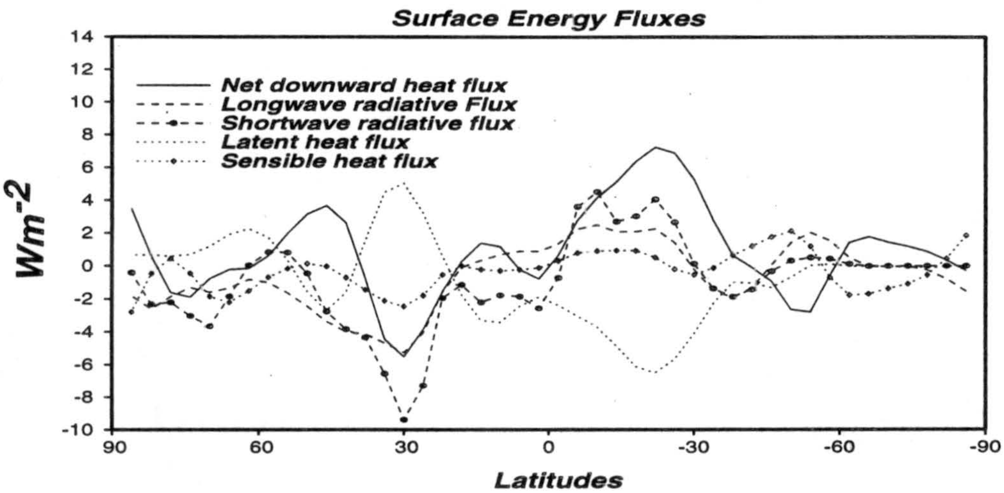

Figure 19: Zonally averaged distributions of the difference of the monthly averaged net downward surface flux, surface longwave radiative flux, surface shortwave radiative flux, surface latent heat flux and surface sensible heat flux simulated with CONTROL and CUPDW. Units are W m^{-2}.

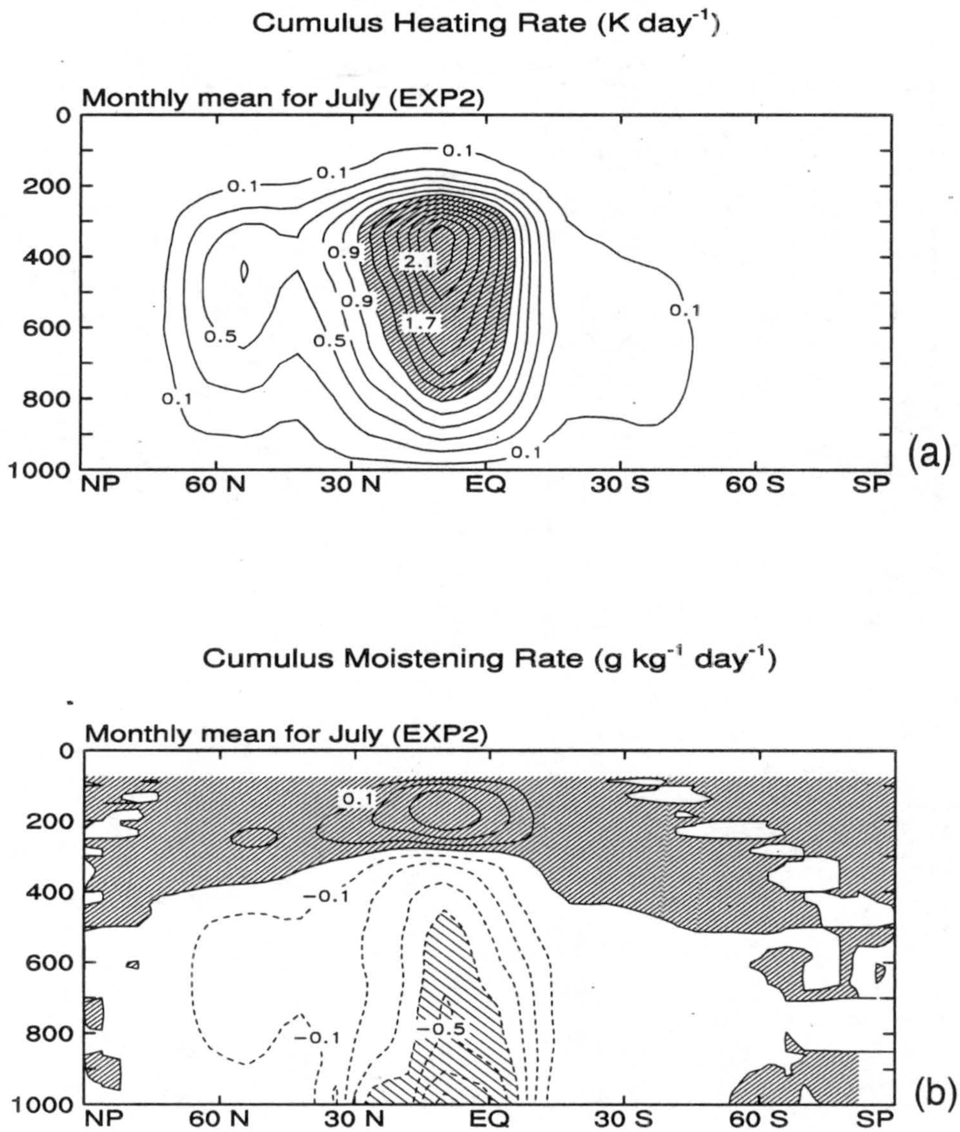

Figure 20: Latitudes-pressure cross sections of the monthly mean cumulus heating rates (a) and moistening rates (b) simulated by EXP2. Units are K day^{-1} in (a) and g kg^{-1} day^{-1}. Heavy shading corresponds to values greater than 1.1 in (a) and 0. in (b). Light shading in (b) corresponds to values less than -0.4.

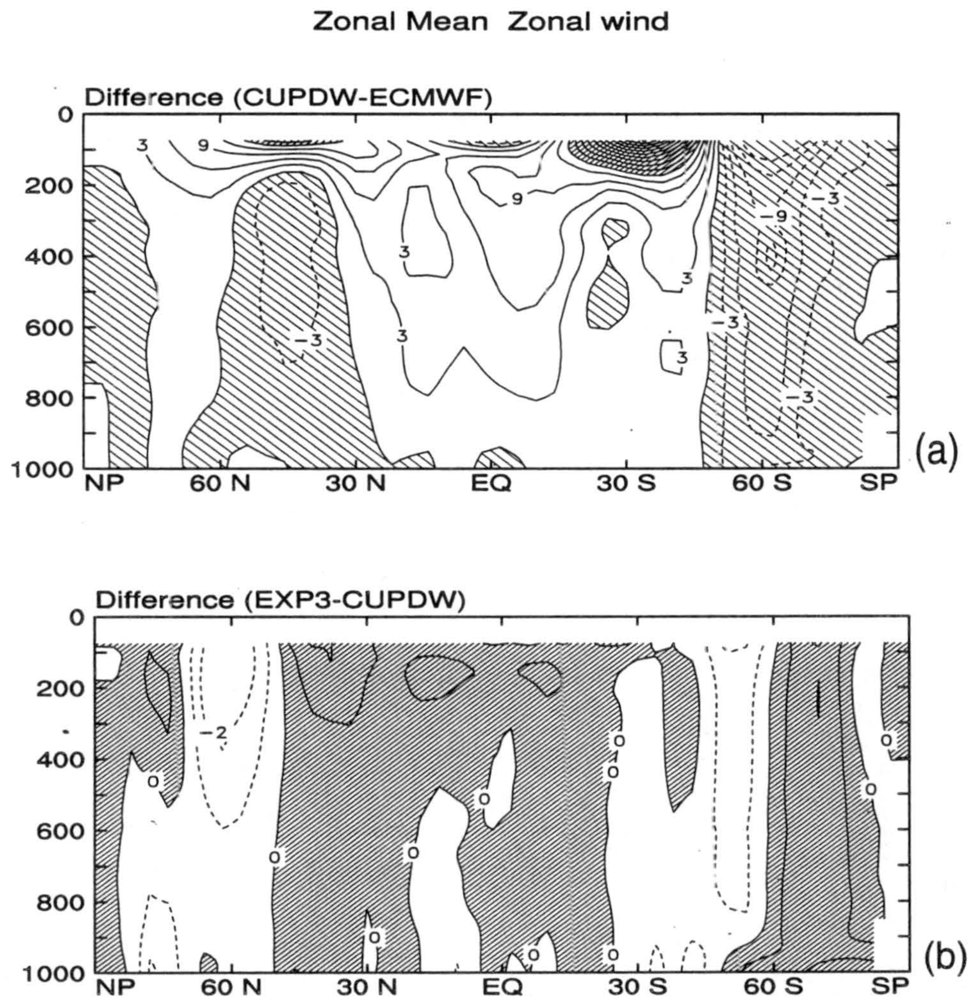

Figure 21: Difference plots of zonal mean zonal wind between CUPDW and ECMWF (a), EXP3 and CUPDW (b). Units are m s^{-1}. Heavy shading in (b) corresponds to value greater than 0. Light shading in (a) corresponds to values less than 0.

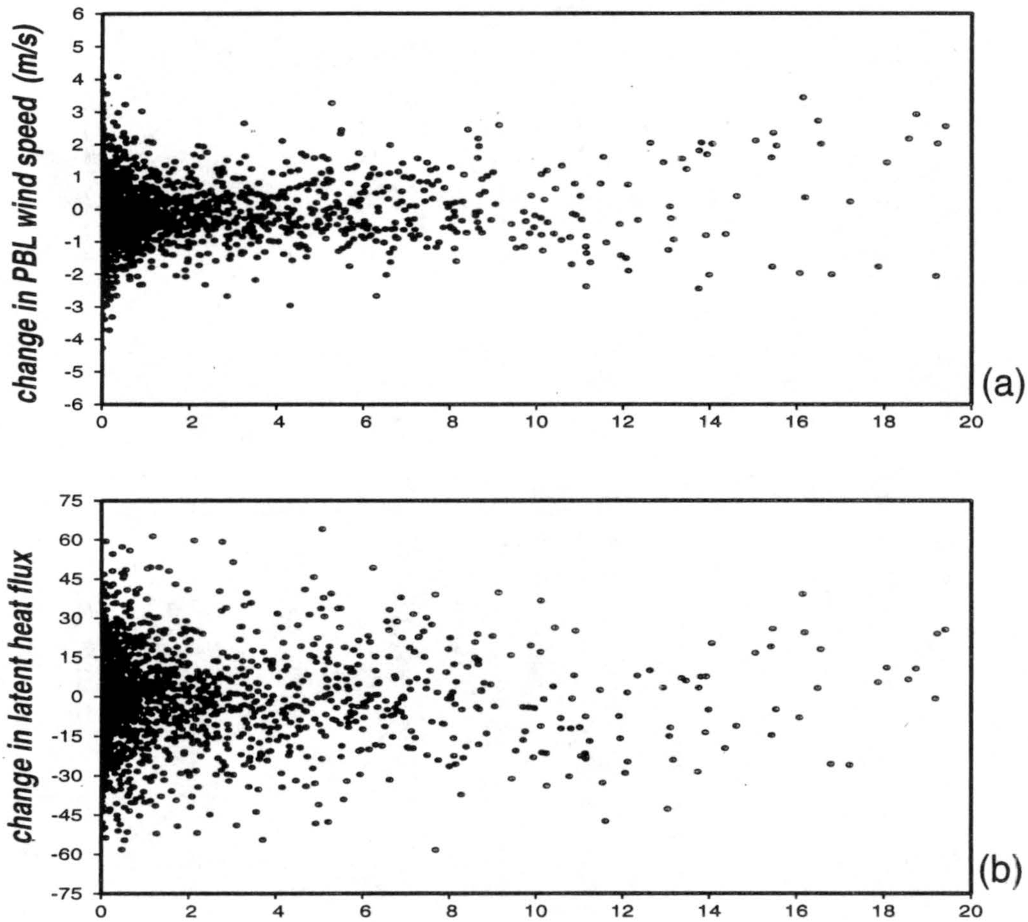

Figure 22: Global scatter diagram: change in PBL wind speed (a) and latent heat flux (b) between EXP3 and CUPDW vs. cumulus precipitation in CUPDW.

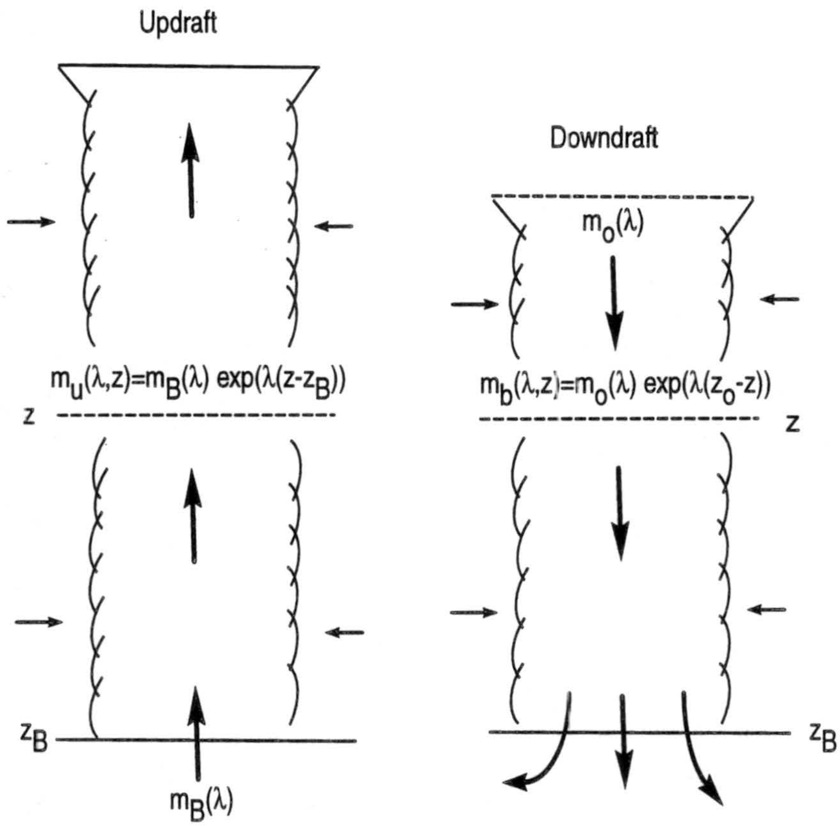

Figure 23: Model for updraft and downdraft of cloud type λ, based on Johnson (1976).

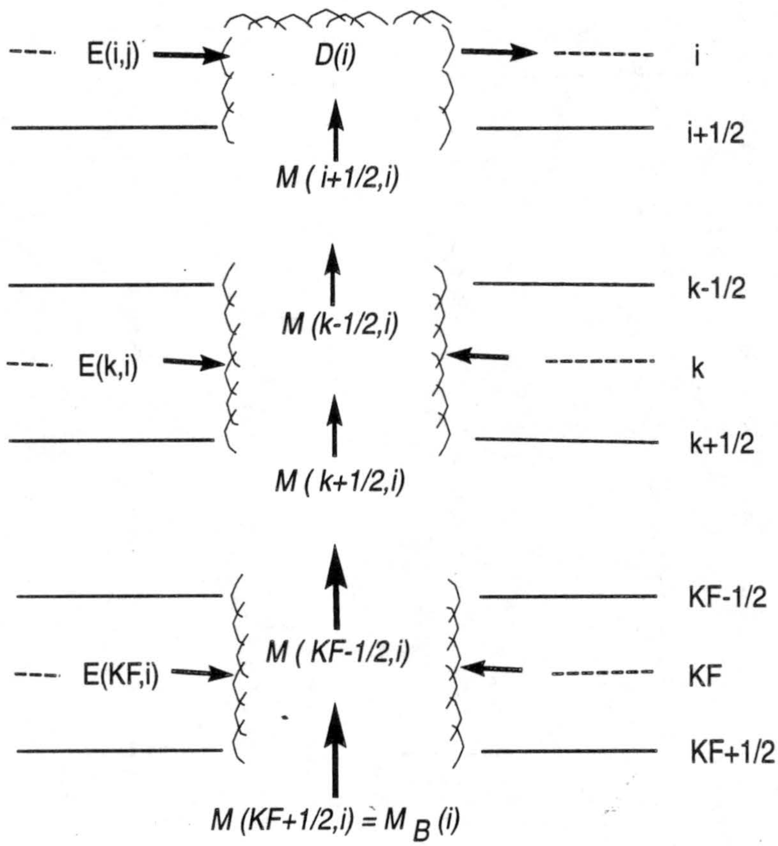

Figure 24: The vertical structure of the ith cloud type, based on Lord et al. (1982). Entrainment E takes place at all integer levels including the cloud-top level, while detrainment D takes place at the cloud-top level only. The sub-ensemble vertical mass flux M is stored at the half-integer and is normalized at cloud base (level $KF + 1/2$).

640033